Revisiting Deep Feature Reconstruction for Logical and Structural Industrial Anomaly Detection

Sukanya Patra *sukanya.patra@umons.ac.be*
University of Mons

Souhaib Ben Taieb *souhaib.bentaieb@mbzuai.ac.ae*
Mohamed bin Zayed University of Artificial Intelligence
University of Mons

Reviewed on OpenReview: *https://openreview.net/forum?id=kdTC4ktHPD*

Abstract

Industrial anomaly detection is crucial for quality control and predictive maintenance, but it presents challenges due to limited training data, diverse anomaly types, and external factors that alter object appearances. Existing methods commonly detect structural anomalies, such as dents and scratches, by leveraging multi-scale features from image patches extracted through deep pre-trained networks. However, significant memory and computational demands often limit their practical application. Additionally, detecting logical anomalies—such as images with missing or excess elements—requires an understanding of spatial relationships that traditional patch-based methods fail to capture. In this work, we address these limitations by focusing on Deep Feature Reconstruction (DFR), a memory- and compute-efficient approach for detecting structural anomalies. We further enhance DFR into a unified framework, called ULSAD, which is capable of detecting both structural and logical anomalies. Specifically, we refine the DFR training objective to improve performance in structural anomaly detection, while introducing an attention-based loss mechanism using a global autoencoder-like network to handle logical anomaly detection. Our empirical evaluation across five benchmark datasets demonstrates the performance of ULSAD in detecting and localizing both structural and logical anomalies, outperforming eight state-of-the-art methods. An extensive ablation study further highlights the contribution of each component to the overall performance improvement. Our code is available at https://github.com/sukanyapatra1997/ULSAD-2024.git.

1 Introduction

Anomaly detection (AD) is a widely studied problem in many fields that is used to identify rare events or unusual patterns (Salehi et al., 2022). It enables the detection of abnormalities, potential threats, or critical system failures across diverse applications such as predictive maintenance (PdM) (Tang et al., 2020; Choi et al., 2022), fraud detection (Ahmed et al., 2016; Hilal et al., 2022), and medicine (Tibshirani & Hastie, 2007; Fernando et al., 2021). Despite its importance and widespread applicability, it remains a challenging task as characterising anomalous behaviours is difficult and the anomalous samples are not known a priori (Ruff et al., 2021). Therefore, AD is often defined as an unsupervised representation learning problem (Pang et al., 2020; Reiss et al., 2022) where the training data contains predominantly normal samples. The aim is to learn the normal behaviour using the samples in the training set and identify anomalies as deviations from this normal behaviour. This setting is also known as one-class classification (Ruff et al., 2018).

Our study focuses on Industrial Anomaly Detection (IAD) (Bergmann et al., 2019), with an emphasis on the detection of anomalies in images from industrial manufacturing processes. Image-based IAD methods assign an anomaly score to each image. Further, this study looks into anomaly localization where each pixel of an image is assigned an anomaly score. It enables fine-grained localization of the anomalous regions in the image. Over the years, it has attracted attention from both industry and academia as AD can be used for various tasks like quality control or predictive maintenance, which are of primal interest to industries. Despite the

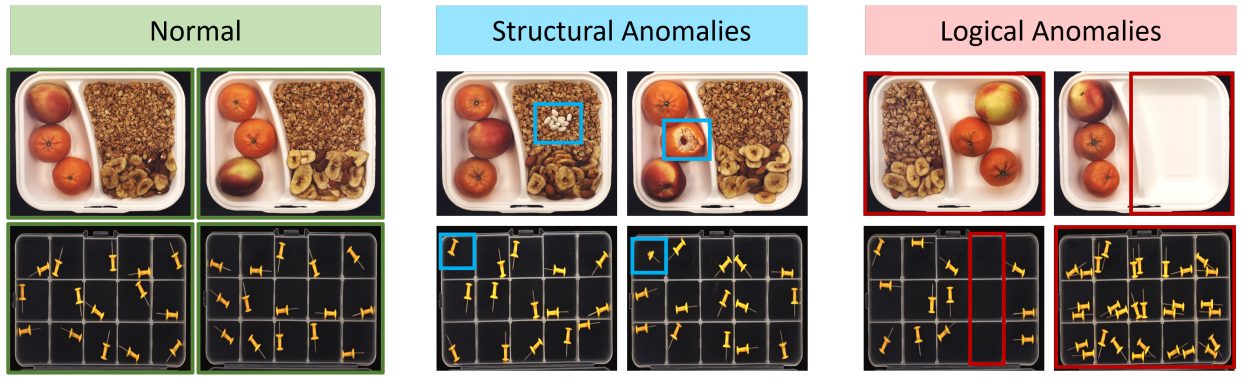

Figure 1: Types of anomalies for the categories "breakfast box" and "pushpin" in MVTecLOCO dataset. Two normal samples (Left) along with structural (Middle) and logical anomalies (Right) where the anomalous regions are highlighted in blue and red, respectively.

necessity, addressing IAD is challenging because: (i) evolving processes result in different manifestations of anomaly (Gao et al., 2023), and (ii) object appearances vary due to external factors such as background, lighting conditions and orientation (Jezek et al., 2021). Furthermore, the anomalies in IAD can be broadly categorized into: (i) **structural anomalies** where subtle localized structural defects can be observed in the images (Bergmann et al., 2019), and (ii) **logical anomalies** where violations of logical constraints result in anomalies (Bergmann et al., 2022). Figure 1 shows examples of both structural and logical anomalies in industrial images.

To detect **structural anomalies**, state-of-the-art methods divides the image into smaller patches and leverage multi-scale features of the image patches obtained using deep convolutional neural networks (Salehi et al., 2021). PatchCore (Roth et al., 2022) and CFA(Lee et al., 2022) achieved state-of-the-art (SOTA) performance by storing the extracted features in a memory bank during the training phase and comparing the features of the image with their closest neighbour from the memory bank during inference. However, such approaches require considerable storage to accumulate the extracted features, which can be challenging for large-scale datasets. The first alternative is knowledge distillation-based approaches (Bergmann et al., 2020; 2022), where a student network is trained to mimic the teacher for normal samples. During inference, anomalies are identified based on the discrepancy between the student and teacher output. A key requirement of these distillation-based approaches is that the student network must be less expressive than the teacher to prevent it from mimicking the teacher on anomalous samples. Thus, regularization methods, such as penalty based on an external dataset or hard-mining loss (Batzner et al., 2024) are applied, that slows down the training and increases the requirement of computing resources. Moreover, excessive regularization can prevent learning representations for normal images. The second alternative is to model the features of normal images using a multivariate Gaussian distribution (Defard et al., 2021) or learn to reconstruct the features using a deep feature reconstruction (DFR) network (Yang et al., 2020).

Besides structural anomalies, **logical anomalies** occur when elements in the images are missing, misplaced, in surplus or violate geometrical constraints (Bergmann et al., 2022). Methods relying on multi-scale features of image patches would fail as they would still be considered normal. It is the combination of objects in the image that makes the image anomalous. Thus, to detect such logical anomalies, it is necessary to look beyond image patches and develop a global understanding of the spatial relationships within normal images. Distillation-based methods, which are predominantly used for the detection of logical anomalies, rely on an additional network to learn the spatial relationships between items in the normal image (Batzner et al., 2024).

In this paper, we focus on DFR, the benefits of which are four-fold. First, it does not need large memory for storing the features, unlike PatchCore (Roth et al., 2022). Second, unlike PaDiM (Defard et al., 2021), it does not make any assumption about the distribution of features. Third, learning to reconstruct features in the latent space of a pre-trained network is less impacted by the curse of dimensionality than learning to reconstruct images which are high-dimensional. Fourth, deep networks trained to reconstruct normal images using the per-pixel distance suffer from the loss of sharp edges of the objects or textures in the background.

As a consequence, AD performance deteriorates due to an increase in false positives, i.e., the number of normal samples falsely labelled anomalies. On the contrary, computing the distance features maps and their corresponding reconstructions during training is less likely to result in such errors (Assran et al., 2023).

We revisit DFR to develop a unified framework for the detection of both structural and logical anomalies. First, we modify the training objective by considering a combination of ℓ_2 and cosine distances between each feature and the corresponding reconstruction. The incorporation of the cosine distance addresses the curse of dimensionality, where high-dimensional features become orthogonal to each other in Euclidean space and the notion of distance disappears (Aggarwal et al., 2001). Second, to simultaneously allow for the detection of logical anomalies, we introduce an attention-based loss using a global autoencoder-like network. We empirically demonstrate that with our proposed changes, not only do the detection and localization capabilities of DFR improve for structural anomalies, but also it delivers competitive results on the detection of logical anomalies. Our contributions can be summarized as:

- Building on DFR, we propose a **U**nified framework for **L**ogical and **S**tructural **A**nomaly **D**etection referred as `ULSAD`, a framework for detection and localization of both structural and logical anomalies.
- To detect structural anomalies, we consider both magnitude and angular differences between the extracted and reconstructed feature vectors.
- To detect logical anomalies, we propose a novel attention-based loss for learning the logical constraints.
- We demonstrate the effectiveness of `ULSAD` by comparing it with 8 SOTA methods across 5 widely adopted IAD benchmark datasets.
- Through extensive ablation study, we show the effect of each component of `ULSAD` on the overall performance of the end-to-end architecture.

2 Related Work

Several methods have been proposed over the years for addressing Industrial AD (Bergmann et al., 2019; 2022; Jezek et al., 2021). They can be broadly categorized into feature-embedding based and reconstruction-based methods. We briefly highlight some relevant works in each of the category. For an extended discussion on the prior works we refer the readers to the survey by Liu et al. (2024).

Feature Embedding-based methods. There are mainly three different types of IAD methods which utilize feature embeddings from a pre-trained deep neural network: *memory bank* (Defard et al., 2021; Roth et al., 2022; Lee et al., 2022), *student-teacher* (Zhang et al., 2023; Batzner et al., 2024), and *density-based* (Gudovskiy et al., 2021; Yu et al., 2021). The main idea of *memory bank* methods is to extract features of normal images and store them in a memory bank during the training phase. During the testing phase, the feature of a test image is used as a query to match the stored normal features. There are two main constraints in these methods: *how to learn useful features* and *how to reduce the size of the memory bank*. While PatchCore (Roth et al., 2022) introduces a coreset selection algorithm, CFA (Lee et al., 2022) clusters the features in the memory bank to reduce the size of the memory bank. Nonetheless, the performance of the *memory bank* methods heavily depends on the completeness of the memory bank, which requires a large number of normal images. Moreover, the memory size is often related to the number of training images, which makes these methods not suitable for large datasets or very high-dimensional images. In the *student-teacher* approach, the student network learns to extract features of the normal images, similar to the teacher model. For anomalous images, the features extracted by the student network are different from the teacher network. Batzner et al. (2024) propose to use an autoencoder model in addition to the student network to identify logical anomalies. For leveraging the multiscale feature from the teacher network to detect anomalies at various scales, Deng & Li (2022) propose Reverse Distillation. Zhang et al. (2023) extended it by proposing to utilize two student networks to deal with structural and logical anomalies. Yang et al. (2020) propose to learn a deep neural network for learning to reconstruct the features of the normal images extracted using the pre-trained backbone. For *density-based* methods, first, a model is trained to learn the distribution of the features obtained from normal samples. Then, during inference, anomalies are detected based on the likelihood of features extracted from the test images. PaDiM (Defard et al., 2021) uses

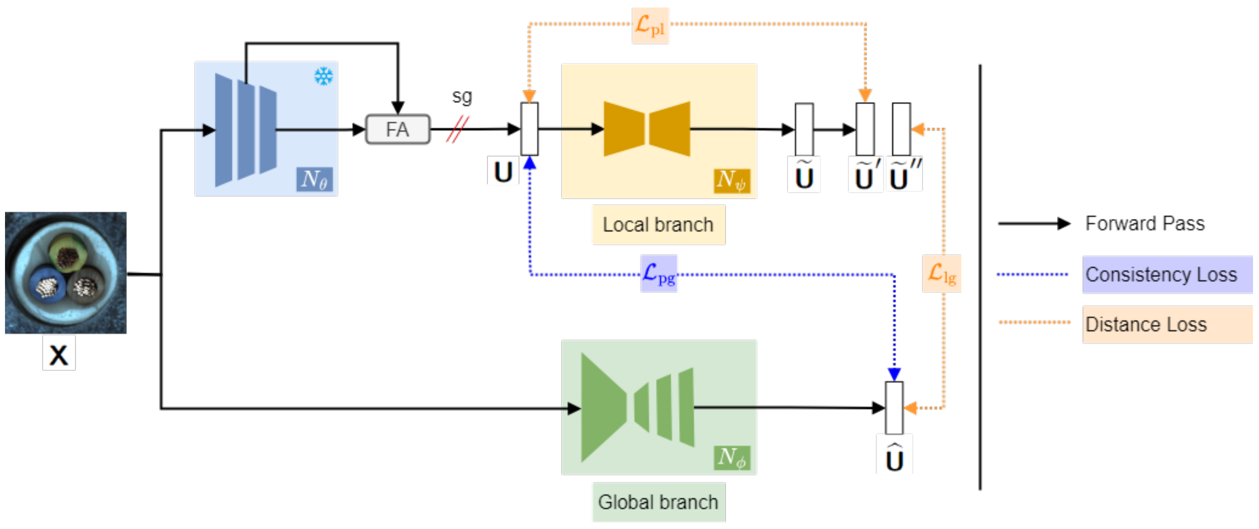

Figure 2: Overview of the end-to-end architecture of `ULSAD`.

a multivariate Gaussian to estimate the density of the features corresponding to the samples from the normal class while FastFlow (Yu et al., 2021) and CFLOW (Gudovskiy et al., 2021) utilize normalizing flows.

Reconstruction-based methods. Reconstruction-based methods assume that encoder-decoder models trained on normal samples will exhibit poor performance for anomalous samples. However, relying solely on the reconstruction objective can result in the model collapsing to an identity mapping. To address this, structural assumptions are made regarding the data generation process. One such assumption is the *Manifold Assumption*, which posits that the observed data resides in a lower-dimensional manifold within the data space. Methods leveraging this assumption impose a bottleneck by restricting the encoded space to a lower dimensionality than the actual data space. Common deep reconstruction models used include AE or VAE-based approaches. Advanced strategies encompass techniques like reconstruction by memorised normality (Gong et al., 2019), model architecture adaptation (Lai et al., 2019) and partial/conditional reconstruction (Yan et al., 2021; Nguyen et al., 2019). Generative models like GANs are also widely employed for anomaly detection, as the discriminator inherently calculates the reconstruction loss for samples (Zenati et al., 2018). Variants of GANs, such as denoising GANs (Sabokrou et al., 2018) and class-conditional GANs (Perera et al., 2019), improve anomaly detection performance by increasing the challenge of reconstruction. Some methods utilize the reconstructed data from GANs in downstream tasks to enhance the amplification of reconstruction errors for anomaly detection (Zhou et al., 2020). Lastly, DRÆM (Zavrtanik et al., 2021) trains an additional discriminative network alongside a reconstruction network to improve the AD performance.

In this paper, we focus on feature embedding-based methods motivated by their effectiveness in the current SOTA methods. Specifically, we build on DFR (Yang et al., 2020), which has several benefits. First, it is memory-efficient as it does not rely on a memory bank of extracted features, unlike PatchCore (Roth et al., 2022). Second, unlike PaDim (Defard et al., 2021), it does not make any assumption about the distribution of the extracted features. Third, it is computationally efficient and less impacted by the curse of dimensionality as it operates in the lower-dimensional latent space of a deep neural network. Last, by avoiding the use of per-pixel distance in its reconstruction objective, it is less prone to false positives (Assran et al., 2023).

3 The `ULSAD` Framework for Anomaly Detection

We propose `ULSAD`, a framework for simultaneously detection and localization of anomalies in images as shown in Figure 2. Firstly, we utilize a feature extractor network for extracting low-dimensional features from high-dimensional images, which we discuss in Section 3.1. Then, for the detection of both structural and logical anomalies, we rely on a dual-branch architecture. The local branch detects structural anomalies with the help of a feature reconstruction network applied to the features corresponding to patches in the image. We elaborate on this in Section 3.2. Conversely, the global branch, as discussed in Section 3.3, detects logical anomalies using an autoencoder-like network, which takes as input the image. Lastly, we provide an overview of the `ULSAD` algorithm in Section 3.4 followed by a discussion on the inference process in Section 3.5.

We consider a dataset $\mathcal{D} = \{(\mathbf{X}_i, y_i)\}_{i=1}^n$ with n samples where $\mathbf{X}_i \in \mathcal{X}$ is an image and $y_i \in \{0, 1\}$ is the corresponding label. We refer to the normal class with the label 0 and the anomalous class with the label 1. The samples belonging to the anomalous class can contain either logical or structural anomalies. We denote the train, validation and test partitions of $\mathcal{D}$ as $\mathcal{D}_{\text{train}}$, $\mathcal{D}_{\text{valid}}$ and $\mathcal{D}_{\text{test}}$, respectively. The training and validation sets contains only normal samples, i.e., $y = 0$. For the sake of simplicity, we refer to the training set as $\mathcal{D}_N = \{\mathbf{X} \mid (\mathbf{X}, 0) \in \mathcal{D}_{\text{train}}\}$. The test set $\mathcal{D}_{\text{test}}$ includes both normal and anomalous samples.

3.1 Feature Extractor

High-dimensional images pose a significant challenge for AD (Reiss et al., 2022). Recent studies have shown that deep convolutional neural networks (CNNs) trained on ImageNet (Russakovsky et al., 2015) capture discriminative features for several downstream tasks. Typically, AD methods (Salehi et al., 2021; Defard et al., 2021; Yoon et al., 2023) leverage such pre-trained networks to extract features maps corresponding to partially overlapping regions or patches in the images. Learning to detect anomalies using the lower-dimensional features is beneficial as it results in reduced computational complexity. A key factor determining the efficiency of such methods is the size of the image patches being used, as anomalies can occur at any scale. To overcome this challenge, feature maps are extracted from multiple layers of the CNNs and fused together (Salehi et al., 2021; Roth et al., 2022; Yang et al., 2020). Each element in a feature map obtained from different layers of a convolutional network corresponds to a patch of a different size in the image depending on its receptive field. Thus, combining feature maps from multiple layers results in multi-scale representation of the image patches, which we refer to as **patch features**.

Similar to DFR, we extract low-dimensional feature maps by combining features from multiple layers of a feature extractor which is a pre-trained CNN N_θ parameterized by θ. In this paper, we consider ResNet-like architectures for N_θ. With the increasing number of layers, the computation becomes increasingly expensive as the resulting tensor becomes high-dimensional. In order to overcome this, we consider two intermediate or mid-level features. Our choice is guided by the understanding that the initial layers of such deep networks capture generic image features, while the latter layers are often biased towards the pre-training classification task (Roth et al., 2022). We denote the features extracted at a layer j for an image $\mathbf{X}$ as $N_\theta^j(\mathbf{X})$. Following this convention, we express the feature map $\mathbf{U} \in \mathcal{U} = \mathbb{R}^{c^* \times h^* \times w^*}$ produced by the *Feature Aggregator* (FA) as a concatenation of $N_\theta^j(\mathbf{X})$ and $N_\theta^{j+1}(\mathbf{X})$ obtained from layers j and $j+1$ of N_θ. Furthermore, to facilitate the concatenation of features extracted from multiple layers of the extractor N_θ, the features at the lower resolution layer $j+1$ are linearly rescaled by FA to match the dimension of the features at layer j. We define an invertible transformation $f : \mathbb{R}^{c^* \times h^* \times w^*} \rightarrow \mathbb{R}^{c^* \times k^*}$ where $k^* = h^* \times w^*$ to convert tensor to matrix and vice versa using f^{-1}. The function f can be computed in practice by reshaping the tensor to obtain a 2D matrix. Now, using f, we compute $\boldsymbol{Z} = f(\mathbf{U})$. We denote each patch feature within the feature map $\boldsymbol{Z}$ by $\boldsymbol{z}_k = \boldsymbol{Z}[:, k] = \mathbf{U}[:, h, w]$, where $k = (h-1) \times w^* + w$, $h \in \{1, 2, \ldots, h^*\}$, $w \in \{1, 2, \ldots, w^*\}$.

3.2 Detecting Structural Anomalies

Having defined $\boldsymbol{Z}$ in the previous section, we elaborate on the local branch of `ULSAD` for the detection of subtle localized defects in the images, i.e. structural anomalies. Specifically, our goal is to learn the reconstruction of the patch features using the dataset $\mathcal{D}_N$ composed of only normal images. Therefore, we can identify the structural anomalies when the network fails to reconstruct a patch feature during inference.

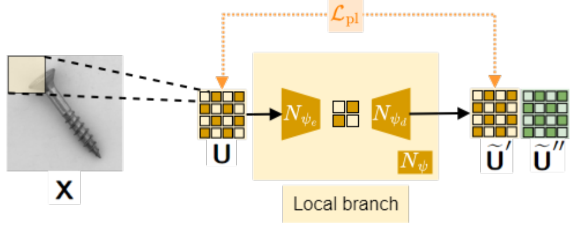

$\mathcal{L}_{\text{pl}}$
$\mathbf{X}$
$\mathbf{U}$
N_{ψ_e}
N_{ψ_d}
N_ψ
$\widetilde{\mathbf{U}}'$
$\widetilde{\mathbf{U}}''$
Local branch

Figure 3: Feature Reconstruction Network

Feature Reconstruction Network (FRN). As shown in Figure 3, `ULSAD` utilizes a convolutional encoder-decoder architecture with a lower-dimensional bottleneck for learning to reconstruct the feature map $\mathbf{U}$ using the training dataset $\mathcal{D}_N$. First, the encoder network N_{ψ_e} compresses the feature $\mathbf{U}$ to a lower dimensional space, which induces the information bottleneck. It acts as an implicit regularizer, preventing generalization to features corresponding to anomalous images. The encoded representation is then mapped back to the latent space using a decoder network N_{ψ_d}. The output of FRN is $\widetilde{\mathbf{U}} = N_\psi(\mathbf{U}) \in \mathbb{R}^{2c^* \times h^* \times w^*}$ where $N_\psi = N_{\psi_e} \circ N_{\psi_d}$. Besides using the FRN to learn the reconstruction of the patch features for the detection of structural anomalies, we also utilize it to reduce errors during the detection of logical anomalies, as discussed in Section 3.3. To minimizing computation costs and avoid the use of two separate FRNs, we adopt a shared FRN. This is achieved by doubling the number of output channels in the decoder to simultaneously produce two feature maps $\widetilde{\mathbf{U}}'$ and $\widetilde{\mathbf{U}}''$ for the detection of structural and logical anomalies, respectively, with both having dimension $c^* \times h^* \times w^*$.

Although the feature maps $\mathbf{U}$ have significantly lower dimensionality compared to the input images $\mathbf{X}$, they can still be considered high-dimensional tensors. In high-dimensional spaces, the ℓ_2 distance is not effective at distinguishing between the nearest and furthest points (Aggarwal et al., 2001), making it an inadequate measure for computing the difference between feature maps during training. Therefore, similar to Salehi et al. (2021), we propose combining ℓ_2 and cosine distances to account for differences in both the magnitude and direction of the patch features as:

$$\mathcal{L}_{\text{pl}}(\widetilde{\boldsymbol{Z}}', \boldsymbol{Z}) = \frac{1}{k^*} \sum_{k=1}^{k^*} l_v(\widetilde{\boldsymbol{z}}'_k, \boldsymbol{z}_k) + \lambda_l \, l_d(\widetilde{\boldsymbol{z}}'_k, \boldsymbol{z}_k), \tag{1}$$

where $\widetilde{\boldsymbol{Z}}' = f(\widetilde{\mathbf{U}}')$, $\boldsymbol{Z} = f(\boldsymbol{Z})$ and $\lambda_l \geq 0$ controls the effect of l_d. Furthermore, $l_v(\widetilde{\boldsymbol{z}}'_k, \boldsymbol{z}_k)$ and $l_d(\widetilde{\boldsymbol{z}}'_k, \boldsymbol{z}_k)$ measure the differences in magnitude and direction between the patch features $\boldsymbol{z}_k$ and $\widetilde{\boldsymbol{z}}'_k$, respectively, as

$$l_v(\widetilde{\boldsymbol{z}}'_k, \boldsymbol{z}_k) = \|\widetilde{\boldsymbol{z}}'_k - \boldsymbol{z}_k\|_2^2, \quad \text{and} \quad l_d(\widetilde{\boldsymbol{z}}'_k, \boldsymbol{z}_k) = 1 - \frac{(\widetilde{\boldsymbol{z}}'_k)^T \boldsymbol{z}_k}{\|\widetilde{\boldsymbol{z}}'_k\|_2 \|\boldsymbol{z}_k\|_2}. \tag{2}$$

3.3 Detecting Logical Anomalies

Although the feature reconstruction task discussed in Section 3.2 allows us to detect structural anomalies, it is not suited for identifying logical anomalies that violate the logical constraints of normal images. Recall that such violations appear in the form of misplaced, misaligned, or surplus objects found in normal images. If we consider the example of misaligned objects, the previously discussed approach will fail as it focuses on the individual image patches, which would be normal. It is the overall spatial arrangement of objects in the image which is anomalous. Thus, to identify such anomalies, our goal is to learn the spatial relationships among the objects present in the normal images of the training dataset $\mathcal{D}_N$. We achieve this with the global branch of `ULSAD`, shown in Figure 4, which leverages the entire image and not just its individual patches.

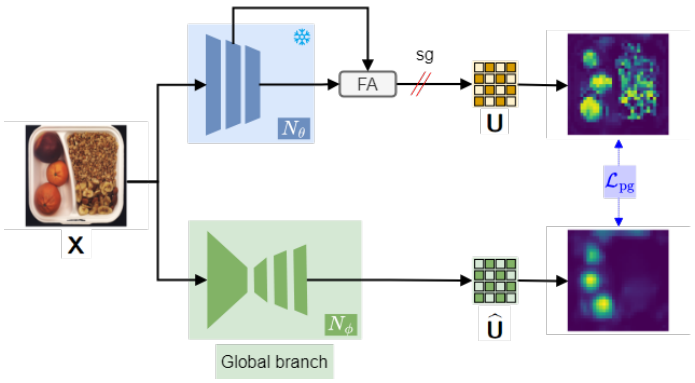

Figure 4: Global Branch of `ULSAD`

In order to achieve our goal, we start by analyzing the feature maps extracted using the pre-trained network N_θ. Pre-trained CNNs tend to have similar activation patterns for semantically similar objects (Tung & Mori, 2019; Zagoruyko & Komodakis, 2017). In Figure 5, we visualize four self-attention maps computed from the features of a pre-trained Wide-Resnet50-2 network. It can be seen that in the first map, all the items for the semantic class "fruits" receive a high attention score. The remaining attention maps focus on individual semantic concepts like "oranges", "cereal" and "plate", respectively. Based on this observation and inspired by the attention-transfer concept for knowledge distillation (Zagoruyko & Komodakis, 2017; Tung & Mori, 2019), we propose to learn the spatial relationships (Dosovitskiy et al., 2021) among the patch features in $\mathbf{U}$ obtained from normal images. Recall that each patch feature corresponds to a patch in the image. Therefore, learning the spatial relationships among the patch features would allow us to learn the spatial relationships among the patches in the image. This forces `ULSAD` to learn the relative positions of objects in

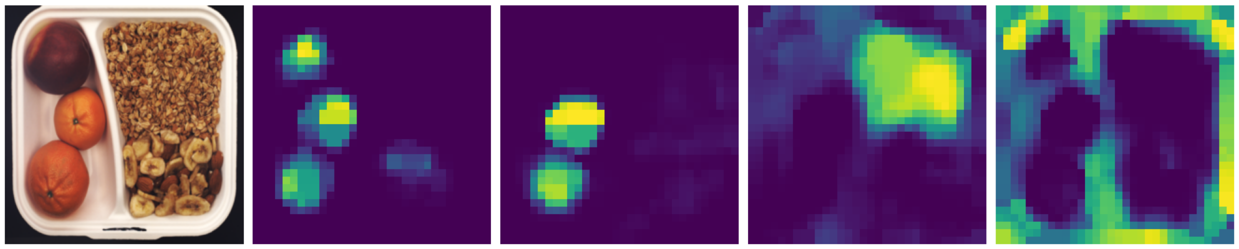

Figure 5: (First) Example image belonging to the category "breakfast box" in the MVTecLOCO dataset. (Rest) Visualization of attention maps computed using the intermediate features from a pre-trained model.

the normal images, thereby enabling it to capture the logical constraints. Starting from $\boldsymbol{Z} = f(\mathbf{U})$, we first compute the self-attention weight matrix $\boldsymbol{W} \in \mathbb{R}^{k^* \times k^*}$ as:

$$\boldsymbol{W}[p,q] = \frac{\exp(\boldsymbol{z}_p^T \ \boldsymbol{z}_q/\sqrt{c^*})}{\sum_{k=1}^{k^*} \exp(\boldsymbol{z}_k^T \ \boldsymbol{z}_q/\sqrt{c^*})}. \tag{3}$$

Then, the attention map $\boldsymbol{A} \in \mathbb{R}^{c^* \times k^*}$ is computed as $\boldsymbol{A} = \boldsymbol{Z}\boldsymbol{W}$. For learning the spatial relations using $\boldsymbol{A}$ as our target, we use a convolutional autoencoder-like network $N_\phi = N_{\phi_e} \circ N_{\phi_d}$ where N_{ϕ_e} is the encoder and N_{ϕ_d} is the decoder. Similar to a standard autoencoder, N_{ϕ_e} compresses the input image $\mathbf{X}$ to a lower dimensional space. However, N_{ϕ_d} maps the encoded representation to the feature space $\mathcal{U}$, which has a lower dimension than the input space $\mathcal{X}$. We denote the output of N_ϕ as $\widehat{\mathbf{U}} = N_\phi(\mathbf{X})$.

A direct approach would be to compute the self-attention map for $\widehat{\mathbf{U}}$ and minimize its distance from $\boldsymbol{A}$. However, it makes the optimization problem computationally challenging as each vector in $\widehat{\mathbf{U}}$ is coupled with every other vector by the network weights N_ϕ (Zhang et al., 2023). To overcome this, we compute the cross-attention map $\widehat{\boldsymbol{A}} \in \mathbb{R}^{c^* \times k^*}$ between $\mathbf{U}$ and $\widehat{\mathbf{U}}$. Given $\widehat{\mathbf{Z}} = f(\widehat{\mathbf{U}})$, we first compute $\widehat{\boldsymbol{W}}$ as:

$$\widehat{\boldsymbol{W}}[p,q] = \frac{\exp(\boldsymbol{z}_p^T \ \widehat{\boldsymbol{z}}_q/\sqrt{c^*})}{\sum_{k=1}^{k^*} \exp(\boldsymbol{z}_k^T \ \widehat{\boldsymbol{z}}_q/\sqrt{c^*})}. \tag{4}$$

Then, the attention map $\widehat{\boldsymbol{A}}$ can be computed as $\widehat{\boldsymbol{A}} = \boldsymbol{Z}\widehat{\boldsymbol{W}}$. Given, the self-attention map $\boldsymbol{A}$ and the cross-attention map $\widehat{\boldsymbol{A}}$, we define a consistency loss $\mathcal{L}_{\text{pg}}$ as:

$$\mathcal{L}_{\text{pg}}(\widehat{\boldsymbol{A}}, \boldsymbol{A}) = \frac{1}{k^*} \sum_{k=1}^{k*} l_v(\widehat{\boldsymbol{a}}_k, \boldsymbol{a}_k) + \lambda_g \ l_d(\widehat{\boldsymbol{a}}_k, \boldsymbol{a}_k), \tag{5}$$

where $\boldsymbol{a}_k = \boldsymbol{A}[:,k]$, $\widehat{\boldsymbol{a}}_k = \widehat{\boldsymbol{A}}[:,k]$ and $\lambda_g \geq 0$ controls the effect of l_d. A limitation of this approach is that autoencoders usually struggle with generating fine-grained patterns as also observed by prior works (Dosovitskiy & Brox, 2016; Assran et al., 2023). As a result, the global branch is prone to false positives in the presence of sharp edges or heavily textured surfaces due to the loss of high-frequency details. To address this limitation, we utilize the FRN N_ψ in the local branch to learn the output $\widehat{\mathbf{U}}$. Recall that the output of FRN $\widetilde{\mathbf{U}} \in \mathbb{R}^{2c^* \times h^* \times w^*}$ has $2c^*$ number of channels to simultaneously generate two feature maps $\widetilde{\mathbf{U}}'$ and $\widetilde{\mathbf{U}}''$, both having dimension $c^* \times h^* \times w^*$. Out of which, $\widetilde{\mathbf{U}}'$ is used for learning the patch features. Here, we define the loss $\mathcal{L}_{lg}$ to relate the local feature map $\widetilde{\mathbf{U}}''$ with the global feature map $\widehat{\mathbf{U}}$ as:

$$\mathcal{L}_{\text{lg}}(\widetilde{\boldsymbol{Z}}'', \widehat{\boldsymbol{Z}}) = \frac{1}{k^*} \sum_{k=1}^{k^*} l_v(\widetilde{\boldsymbol{z}}''_k, \widehat{\boldsymbol{z}}_k) + \lambda_g \ l_d(\widetilde{\boldsymbol{z}}''_k, \widehat{\boldsymbol{z}}_k), \tag{6}$$

where $\widetilde{\boldsymbol{Z}}'' = f(\widetilde{\mathbf{U}}'')$. Therefore, during inference, a difference between the $\widetilde{\mathbf{U}}''$ and $\widehat{\mathbf{U}}$ indicates the presence of logical anomalies. The benefits of such a framework are two-fold: (1) it allows for learning the spatial relationships in the normal images while reducing the chance of having false positives, and (2) doubling the channels in the decoder allows sharing the encoder architecture, reducing the computational costs.

```
Algorithm 1: Unified Logical and Structural AD (ULSAD) // Local branch  Global branch
Require: Training dataset $\mathcal{D}_N$, Feature extractor $N_\theta$, Feature reconstruction network $N_\psi$
Global autoencoder $N_\phi$, Number of epochs $e$, Learning rate $\eta$, Pre-trained feature statictics $\boldsymbol{\mu}$, $\boldsymbol{\sigma}$
1  for (epoch $\in 1, \cdots, e$) and ($\mathbf{X} \in \mathcal{D}_N$) do
2      Extract normalized features maps using the pre-trained network:
3          $\mathbf{U} \leftarrow N_\theta(\mathbf{X})$
4          $\mathbf{U} \leftarrow (\mathbf{U} - \boldsymbol{\mu})/\boldsymbol{\sigma}$
5          $\boldsymbol{Z} \leftarrow f(\mathbf{U})$
6      Reconstruct the features maps using the local branch:
7          $\widetilde{\mathbf{U}} \leftarrow N_\psi(\mathbf{U})$
8          $\widetilde{\boldsymbol{Z}} \leftarrow f(\widetilde{\mathbf{U}})$
9      Compute local loss (Eq. 1):
10         $l_l \leftarrow \mathcal{L}_{\text{pl}}(\widetilde{\boldsymbol{Z}}', \boldsymbol{Z})$
11     Obtain the output of the global autoencoder:
12         $\widehat{\mathbf{U}} \leftarrow N_\phi(\mathbf{X})$
13         $\widehat{\boldsymbol{Z}} \leftarrow f(\widehat{\mathbf{U}})$
14     Compute consistency loss (Eq. 5):
15         $l_g \leftarrow \mathcal{L}_{pg}(\widehat{\boldsymbol{Z}}, \boldsymbol{Z})$
16     Compute local-global loss (Eq. 6):
17         $l_{\text{lg}} \leftarrow \mathcal{L}_{lg}(\widehat{\boldsymbol{Z}}, \widetilde{\boldsymbol{Z}}'')$
18     Compute overall loss:
19         $l \leftarrow l_l + l_g + l_{\text{lg}}$
20     Update model parameters:
21         $\psi \leftarrow \psi - \eta\nabla_\psi l$
22         $\phi \leftarrow \phi - \eta\nabla_\phi l$
23 end
Return: $N_\psi$, $N_\phi$
```

3.4 ULSAD Algorithm Overview

An overview of ULSAD is outlined in Algorithm 1, which can simultaneously detect structural and logical anomalies. Firstly, we pass a normal image $\mathbf{X}$ from the training dataset $\mathcal{D}_N$ through the feature extractor N_θ to obtain feature maps $\mathbf{U}$. We normalize the features (line 4, Algorithm 1) with the channel-wise mean $\boldsymbol{\mu}$ and standard deviation $\boldsymbol{\sigma}$ computed over all the images in $\mathcal{D}_N$. We do not include this step in Algorithm 1 as the calculation is trivial. Instead, we consider the values $\boldsymbol{\mu}$ and $\boldsymbol{\sigma}$ to be given as input parameters for the sake of simplicity. Secondly, we obtain $\widetilde{\mathbf{U}}$ by passing $\mathbf{U}$ through the feature reconstruction network N_ψ (line 7, Algorithm 1). Recall that, $\widetilde{\mathbf{U}}$ has a dimension $2c^* \times h^* \times w^*$ which can be decomposed into two feature maps $\widetilde{\mathbf{U}}'$ and $\widetilde{\mathbf{U}}''$ each with a dimension $c^* \times h^* \times w^*$. The feature reconstruction loss $\mathcal{L}_{\text{pl}}$ is then computed between $\boldsymbol{Z}$ and $\widetilde{\boldsymbol{Z}}'$, where $\boldsymbol{Z} = f(\mathbf{U})$ and $\widetilde{\boldsymbol{Z}}' = f(\widetilde{\mathbf{U}}')$. Thirdly, we obtain the features $\widehat{\mathbf{U}}$ by passing the input sample $\mathbf{X}$ through the autoencoder N_ϕ. Then for learning the spatial relationships from the normal images, we compute $\mathcal{L}_{\text{pg}}$ between the self-attention map of $\boldsymbol{Z}$ and the cross-attention map between $\boldsymbol{Z}$ and $\widehat{\mathbf{Z}} = f(\widehat{\mathbf{U}})$ (line 15, Algorithm 1). In the fourth step, we compute the loss $\mathcal{L}_{\text{lg}}$ between $\widehat{Z}$ and $\widetilde{\boldsymbol{Z}}'' = f(\widetilde{\mathbf{U}}'')$. Finally, the model parameters ψ and ϕ are updated based on the gradient of the total loss (line $21 - 22$, Algorithm 1). The end-to-end pipeline is illustrated in Figure 2.

3.5 Anomaly Detection and Localization

After discussing how ULSAD is trained to detect structural and logical anomalies, we now focus on the inference process. The first step is to compute an anomaly map $\boldsymbol{M}$ for a given test image $\mathbf{X}$, which assigns a per-pixel anomaly score. We begin by calculating the local anomaly map $\boldsymbol{M}^l \in \mathbb{R}^{h^* \times w^*}$ based on the difference between the output of the local branch $\widetilde{\mathbf{U}}'$ and the feature map $\mathbf{U}$, as follows:

$$\boldsymbol{M}^l[h,w] = l_v(\widetilde{\mathbf{U}}'[:,h,w],\ \mathbf{U}[:,h,w]) + \lambda_l\ l_d(\widetilde{\mathbf{U}}'[:,h,w],\ \mathbf{U}[:,h,w]), \tag{7}$$

where $\widetilde{\mathbf{U}}' = f^{-1}(\widetilde{\boldsymbol{Z}}')$ and $\mathbf{U} = f^{-1}(\boldsymbol{Z})$. Similarly, the global anomaly map $\boldsymbol{M}^g$ is computed using the output from the global autoencoder $\widehat{\mathbf{U}}$ and the local reconstruction branch $\widetilde{\mathbf{U}}''$:

$$\boldsymbol{M}^g[h,w] = l_v(\widetilde{\mathbf{U}}''[:,h,w], \widehat{\mathbf{U}}[:,h,w]) + \lambda_g\ l_d(\widetilde{\mathbf{U}}''[:,h,w], \widehat{\mathbf{U}}[:,h,w]), \tag{8}$$

where $\widetilde{\mathbf{U}}'' = f^{-1}(\widetilde{\boldsymbol{Z}}'')$ and $\widehat{\mathbf{U}} = f^{-1}(\widehat{\boldsymbol{Z}})$.

Since $\boldsymbol{M}^l$ and $\boldsymbol{M}^g$ may have different ranges of anomaly scores, we normalize each map independently. This normalization ensures consistent score ranges and prevents noise in one map from overwhelming anomalies detected in the other. Given the variability in anomaly score distributions across datasets, we adopt a quantile-based normalization method, which makes no assumptions about the underlying score distribution.

To normalize the maps, we generate two sets of anomaly maps: $\mathcal{M}^l = \{\boldsymbol{M}^l \mid \mathbf{X} \in \mathcal{D}_{\text{valid}}\}$ and $\mathcal{M}^g = \{\boldsymbol{M}^g \mid \mathbf{X} \in \mathcal{D}_{\text{valid}}\}$, using images from the validation set $\mathcal{D}_{\text{valid}}$. For each set, we pool together the pixel values from all the anomaly maps in that set to compute the empirical quantiles at significance levels α and β. Specifically, for the local anomaly maps, the quantiles are denoted as q^l_α and q^l_β, while for the global anomaly maps, the quantiles are denoted as q^g_α and q^g_β. Values below q_α are considered normal, while those above q_β are marked as highly abnormal.

Following Batzner et al. (2024), we define linear transformations $t^l(\cdot)$ and $t^g(\cdot)$ for the local and global anomaly maps to map normal pixels to values ≤ 0 and highly anomalous pixels to values ≥ 0.1:

$$t^l(\boldsymbol{M}^l) = 0.1\left(\boldsymbol{M}^l - \left(\frac{q^l_\alpha}{q^l_\beta - q^l_\alpha}\right)\mathbf{1}_{h^*\times w^*}\right), \quad t^g(\boldsymbol{M}^g) = 0.1\left(\boldsymbol{M}^g - \left(\frac{q^g_\alpha}{q^g_\beta - q^g_\alpha}\right)\mathbf{1}_{h^*\times w^*}\right),$$

where $\mathbf{1}_{h^*\times w^*}$ is a matrix of ones. Mapping the empirical quantiles at α and β to values of 0 and 0.1 helps highlight the anomalous regions on a 0-to-1 color scale for visualization. Normal pixels are assigned a score of 0, while pixels with scores between q_α and q_β gradually increase in color intensity. Pixels with scores exceeding q_β change more rapidly toward 1. Note that this transformation does not affect AU-ROC scores, as these depend only on the ranking of the scores.

Finally, we compute the overall anomaly map $\boldsymbol{M}$ for the image $\mathbf{X}$ by averaging the normalized local and global maps:

$$\boldsymbol{M} = \frac{t^l(\boldsymbol{M}^l) + t^g(\boldsymbol{M}^g)}{2}.$$

The final anomaly score for $\mathbf{X}$ is the maximum value in the combined anomaly map:

$$s = \max_{h\in\{1,2,\ldots,h^*\}, w\in\{1,2,\ldots,w^*\}} \boldsymbol{M}(h,w).$$

4 Experimental Evaluation

In this section, we answer the following three questions: (i) How does `ULSAD` perform as compared to the SOTA methods? (ii) How effective is the local and global branch for the detection of *structural* and *logical* anomalies? (iii) How does each component in `ULSAD` impact the overall performance?

4.1 Setup

Benchmark Datasets. We evaluate our method on the following five IAD benchmarking datasets:

[1] BTAD (Mishra et al., 2021). It comprises real-world images of three industrial products, with anomalies such as body and surface defects. Training data includes 1,799 normal images across the three categories, while the test set contains 290 anomalous and 451 normal images.

[2] MVTec AD (Bergmann et al., 2019). It consists of images from industrial manufacturing across 15 categories comprised of 10 objects and 5 textures. In totality, it contains 3,629 normal images for training. For evaluation, 1,258 anomalous images with varying pixel level defects and 467 normal images.

[3] MVTec-Loco (Bergmann et al., 2022). An extension of MVTec dataset, it encompasses both local structural anomalies and logical anomalies violating long-range dependencies. It consists of 5 categories, with 1,772 normal images for training and 304 normal images for validation. It also contains 1568 images, either normal or anomalous, for evaluation.

[4] MPDD (Jezek et al., 2021). It focuses on metal part fabrication defects. The images are captured in variable spatial orientation, position, and distance of multiple objects concerning the camera at different light intensities and with a non-homogeneous background. It consists of 6 classes of metal parts with 888 training images. For evaluation, the dataset has 176 normal and 282 anomalous images.

[5] VisA (Zou et al., 2022). It contains 10,821 high-resolution images (9,621 normal and 1,200 anomalous images) across 12 different categories. The anomalous images contain different types of anomalies such as scratches, bent, cracks, missing parts or misplacements. For each type of defect, there are 15-20 images, and an image can depict multiple defects.

Evaluation metrics. We measure the image-level anomaly detection performance via the area under the receiver operator curve (AUROC) based on the assigned anomaly score. To measure the anomaly localization performance, we use pixel-level AUROC and area under per region overlap curve (AUPRO). Furthermore, following prior works (Roth et al., 2022; Gudovskiy et al., 2021; Bergmann et al., 2019), we compute the average metrics over all the categories for each of the benchmark datasets. Moreover, for `ULSAD`, we report all the results over 5 runs with different random seeds.

Baselines. We compare our method with existing state-of-the-art unsupervised AD methods, namely PatchCore (Roth et al., 2022), PaDim (Defard et al., 2021), CFLOW (Gudovskiy et al., 2021), FastFLOW (Yu et al., 2021), DRÆM (Zavrtanik et al., 2021), Reverse Distillation (RD) (Deng & Li, 2022), EfficientAD (Batzner et al., 2024) and DFR (Yang et al., 2020). In this study, we only consider baselines that are capable of both anomaly detection and localization.

Implementation details. `ULSAD` is implemented in PyTorch (Paszke et al., 2019). For the baselines, we follow the implementation in Anomalib (Akcay et al., 2022), a widely used AD library for benchmarking. In `ULSAD`, we use a Wide-ResNet50-2 pre-trained on ImageNet (Zagoruyko & Komodakis, 2016) and extract features from the second and third layers, similar to PathCore (Roth et al., 2022). We use a CNN for the autoencoder N_ϕ in the global branch and the feature reconstruction network N_ψ in the local branch. It consists of convolution layers with LeakyReLU activation in the encoder and deconvolution layers in the decoder. The architecture is provided in the Appendix A. Unless otherwise stated, for all the experiments, we consider an image size of 256×256. We train `ULSAD` over 200 epochs for each category using an Adam optimizer with a learning rate of 0.0002 and a weight decay of 0.00002. We set $\alpha = 0.9$ and $\beta = 0.995$ unless specified otherwise. For the baselines, we use the hyperparameters mentioned in the respective papers.

4.2 Evaluation Results

We summarize the anomaly detection performance of `ULSAD` in Table 1 and the localization performance in Table 2. On the BTAD dataset, we improve over the DFR by approximately 2% in detection. Inspecting the images from the dataset, we hypothesize that the difference stems from the use of a global branch in `ULSAD` as the structural imperfections are not limited to small regions. For localization, Reverse Distillation performs better owing to the use of anomaly maps computed per layer of the network. We can observe similar improvements over DFR on the MVTec dataset. Although PatchCore provides superior performance on MVTec, it should be noted that even without using a memory bank, `ULSAD` provides comparable results. Then, we focus on more challenging datasets such as MPDD and MVTecLOCO. While MPDD contains varying external conditions such as lighting, background and camera angles, MVTecLOCO contains both logical and structural anomalies. We can observe improvements over DFR ($\sim 12 - 16\%$) in both datasets. This highlights the effectiveness of our method. We visualize the anomaly maps for samples from the "pushpin" and "juice bottle" categories in Figure 6. It can be seen that while the global branch is more suited to the detection of logical anomalies, the local branch is capable of detecting localized structural anomalies.

Table 1: Average Detection Performance in AUROC (%). Style: **best** and <u>second best</u>

Method	BTAD	MPDD	MVTec	MVTec-LOCO	VisA
PatchCore (Roth et al., 2022)	93.27	<u>93.27</u>	**98.75**	<u>81.49</u>	<u>91.48</u>
CFLOW (Gudovskiy et al., 2021)	93.57	87.11	94.47	73.62	87.77
DRÆM (Zavrtanik et al., 2021)	73.42	74.14	75.26	62.35	77.75
EfficientAD (Batzner et al., 2024)	88.26	85.42	<u>98.23</u>	80.62	91.21
FastFlow (Yu et al., 2021)	91.68	65.03	90.72	71.00	87.49
PaDiM (Defard et al., 2021)	93.20	68.48	91.25	68.38	83.28
Reverse Distillation (Deng & Li, 2022)	83.87	79.62	79.65	61.56	86.24
DFR (Yang et al., 2020)	<u>94.60</u>	79.75	93.54	72.87	85.18
ULSAD (Ours)	**96.17** ± 0.45	**95.73** ± 0.45	97.65 ± 0.38	**84.1** ± 0.86	**92.46** ± 0.45

Table 2: Average Segmentation Performance in AUROC (%) and AUPRO (%). Style: **best** and <u>second best</u>

Method	BTAD	MPDD	MVTec	MVTec-LOCO	VisA
PatchCore (Roth et al., 2022)	96.85 | 71.48	**98.07** | 90.84	**97.71** | 91.15	75.77 | 69.09	97.93 | 85.12
CFLOW (Gudovskiy et al., 2021)	96.60 | 73.11	97.42 | 88.56	97.17 | 90.14	<u>76.99</u> | 66.93	98.04 | 85.29
DRÆM (Zavrtanik et al., 2021)	59.04 | 22.48	86.96 | 70.04	75.01 | 49.72	63.69 | 40.06	71.31 | 54.68
EfficientAD (Batzner et al., 2024)	82.13 | 54.37	97.03 | 90.44	96.29 | 90.11	70.36 | 66.96	97.51 | 84.45
FastFlow (Yu et al., 2021)	96.15 | 75.27	93.60 | 76.89	96.44 | 88.79	75.55 | 53.04	97.32 | 81.70
PaDiM (Defard et al., 2021)	97.07 | <u>77.80</u>	94.51 | 81.18	96.79 | 91.17	71.32 | 67.97	97.09 | 80.80
Reverse Distillation (Deng & Li, 2022)	**97.85** | **81.47**	<u>97.83</u> | <u>91.86</u>	97.25 | **93.12**	68.55 | 66.28	**98.68** | **91.77**
DFR (Yang et al., 2020)	<u>97.62</u> | 59.06	97.33 | 90.46	94.93 | 89.42	61.72 | <u>69.78</u>	97.90 | <u>91.72</u>
ULSAD (Ours)	96.73 | 75.41 ± 0.51 | ± 3.95	97.45 | **92.02** ± 0.99 | ± 2.64	<u>97.61</u> | <u>91.67</u> ± 0.64 | ± 1.36	**80.06** | **73.73** ± 0.20 | ± 0.35	<u>98.24</u> | 87.12 ± 0.20 | ± 0.89

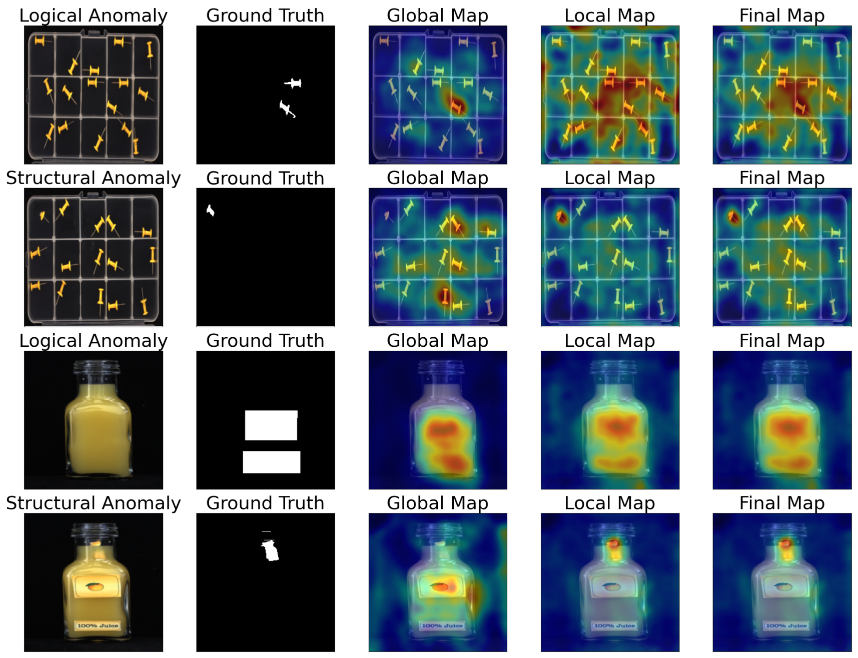

Figure 6: Example of anomaly maps obtained from global and local branches along with the combined map.

Overall, ULSAD demonstrates competitive results in anomaly detection compared to the baseline methods across all benchmark datasets. Additionally, the difference in performance between ULSAD and the baselines for anomaly localization is minimal. The most notable difference is in the AUPRO score on the BTAD, MVTec, and VisA datasets. Nonetheless, while the SOTA methods provide slightly better performance in the localization of structural anomalies, ULSAD provides similar performance across both logical and structural anomalies. We present anomaly maps obtained from different methods in Figure 9 of Appendix B. Extended versions of Tables 1 and 2 are provided in Appendix B. Additionally, we provide the results on MVTecLOCO, split between logical and structural anomalies, in Appendix B.1.

4.3 Ablation study

In this section, we analyze the impact of the key components of ULSAD, backbone architectures and the choice of α and β for normalization, using the MVTecLOCO dataset.

Analysis of main components. We investigate the impact of key components in ULSAD as presented in Table 3. Initially, we set both λ_l and λ_g to 0, focusing solely on differences in magnitude when computing $\mathcal{L}_{pg}$, $\mathcal{L}_{lg}$, and $\mathcal{L}_{pl}$. The first row corresponds to using only the local branch. In the third row, the consistency loss $\mathcal{L}_{pg}$ is applied to capture spatial relationships for detecting logical anomalies. However, when used in isolation, it limits ULSAD's performance to detecting only logical anomalies and fails to capture localized structural anomalies. Additionally, as discussed in Section 3.3, the global branch is prone to false positives in the presence of sharp edges or heavily textured surfaces. When incorporating $\mathcal{L}_{lg}$, which connects the global and local branches, we observe a significant improvement in performance, as shown in the fifth row. For the sake of completeness, we also consider here a variant of the consistency loss $\mathcal{L}_{\text{pg}}$ where we compute the ℓ_2 distance between the feature maps instead of computing the self- and cross-attention maps. We refer to the alternative in the table as $\mathcal{L}^d_{\text{pg}}$. We observe that the difference between the two variants becomes negligible when combined with $\mathcal{L}_{lg}$ (row 4 and 5). Further, incorporating differences in direction when computing $\mathcal{L}_{pg}$, $\mathcal{L}_{lg}$, and $\mathcal{L}_{pl}$ leads to improved performances across all settings as shown in the last five rows. Overall, the best performance is obtained when both $\mathcal{L}_{lg}$ and $\mathcal{L}_{pg}$ is used while considering differences in both direction and magnitude for computing the losses.

Table 3: Ablation of the main components of ULSAD.

	Local Branch	Global Branch				Performance (%)
	λ_l	λ_g	$\mathcal{L}_{\text{lg}}$	$\mathcal{L}^d_{\text{pg}}$	$\mathcal{L}_{\text{pg}}$	I-AUROC | P-AUROC | P-AUPRO
1	0.0	-	-	-	-	77.67 | 75.17 | 73.37
2	0.0	0.0	-	✓	-	77.69 | 79.77 | 75.26
3	0.0	0.0	-	-	✓	71.67 | 73.92 | 67.22
4	0.0	0.0	✓	✓	-	81.40 | 82.12 | 77.47
5	0.0	0.0	✓	-	✓	81.08 | 81.97 | 76.45
6	0.5	-	-	-	-	79.14 | 76.57 | 73.41
7	0.5	0.5	-	✓	-	80.50 | 81.85 | 77.35
8	0.5	0.5	-	-	✓	74.51 | 76.59 | 69.01
9	0.5	0.5	✓	✓	-	82.19 | 81.25 | 75.50
10	0.5	0.5	✓	-	✓	**84.10** | **80.06** | **73.73** $\pm$ 0.86 | $\pm$ 0.20 | $\pm$ 0.35

Effect of backbone. We investigate the impact of using different pre-trained backbones in ULSAD in Figure 7. We can observe that the overall best performance is obtained by using a Wide-ResNet101-2 architecture in both detection and localization. More specifically, for detection, Wide-ResNet variants are more effective than the ResNet architectures, whereas, for localization performance measured using Pixel AUROC, the deeper networks such as ResNet152 and Wide-ResNet101-2 seem to have precedence over their shallower counterparts. Overall, we can see that performance is robust to the choice of pre-trained model architecture. In our experiments, we utilize a Wide-ResNet50-2 architecture which is used by most of our baselines for fair comparison.

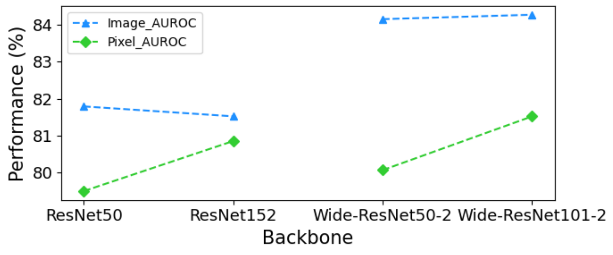

Figure 7: Ablation study of the backbone network

Effect of normalization. We analyze the impact of the quantile-based normalization on the performance metrics by considering multiple values for α and β. The results are shown in Figure 8. It can be seen that the final performance is robust to the choice of α and β.

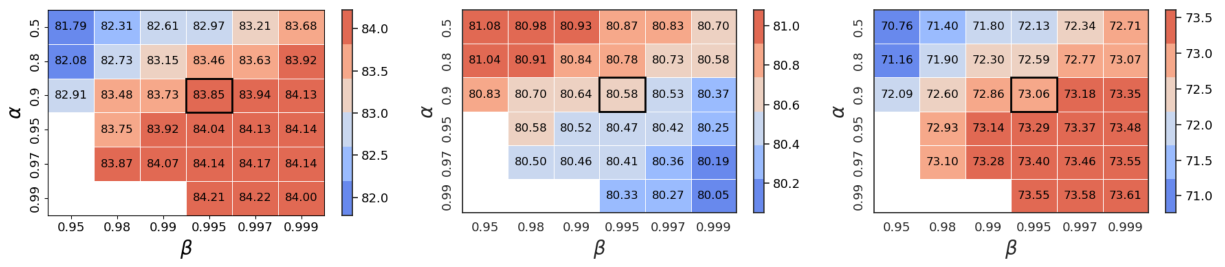

(a) Image AUROC (b) Pixel AUROC (c) Pixel AUPRO

Figure 8: Ablation study of α and β for normalization of anomaly maps with selected value highlighted.

Table 4: Memory and Computational Efficiency on MVTecLOCO dataset.

	CFLOW (2021)	DRÆM (2021)	FastFlow (2021	PaDiM (2021)	PatchCore (2022)	RD (2022)	DFR (2020)	EffAD (2024)	ULSAD (Ours)
I-AUROC ↑	73.62	62.35	71.00	68.38	<u>81.49</u>	61.56	72.87	80.62	**84.10** ± 0.86
P-AUROC ↑	<u>76.99</u>	63.69	75.55	71.32	75.77	68.55	61.72	70.36	**80.06** ± 0.20
P-AUPRO ↑	66.93	40.06	53.04	67.97	69.09	66.28	<u>69.78</u>	66.96	**73.73** ± 0.35
Throughput (img / s) ↑	11.69	10.06	30.21	<u>33.45</u>	32.70	**34.87**	15.08	23.33	33.42
GPU Memory (GB) ↓	2.57	7.95	**1.69**	<u>1.92</u>	6.80	1.93	5.85	3.48	2.17

5 Memory and Computational Complexity

We report the computational cost and memory requirements of ULSAD compared to the baselines in Table 4. For this analysis, we ran inference on the test samples in the MVTecLOCO dataset using an NVIDIA A100 GPU. We measured throughput with a batch size of 32, as a measure of computational complexity, following EfficientAD (Batzner et al., 2024). Throughput is defined as the number of images processed per second when processing in batches. ULSAD demonstrates higher throughput than most baselines while maintaining competitive anomaly detection and localization performance. In addition to throughput, we also report peak GPU memory usage in Table 4 to highlight the memory efficiency of ULSAD. It is evident that ULSAD requires approximately one-third of the memory compared to retrieval-based methods such as PatchCore, which is one of the state-of-the-art methods for IAD. For DFR (Yang et al., 2020), we follow the authors' approach by using a multiscale representation, concatenating features from 12 layers of the pre-trained network N_θ for anomaly detection. This approach results in reduced throughput and increased memory usage, as shown in Table 4. With our proposed modifications in ULSAD, we achieve superior performance using features from only 2 layers of N_θ, drastically reducing memory requirements to approximately one-third of DFR's and increasing throughput by approximately two times.

6 Limitations

For training ULSAD, we follow the common assumption in unsupervised anomaly detection (Ruff et al., 2021; Chandola et al., 2009; Roth et al., 2022; Batzner et al., 2024) that the training dataset is "clean", meaning it contains no anomalous samples. This setup is known in the literature as one-class classification (Ruff et al., 2018). However, this assumption could impact performance in real-world scenarios where anomalies are unknown a priori. Investigating the effects of dataset contamination (Wang et al., 2019; Jiang et al., 2022; Yoon et al., 2022; Perini et al., 2023; 2022) is an active area of research, which is beyond the scope of our current work. We leave for future research the analysis of contamination's impact on ULSAD and the development of strategies to make the learning process robust in the presence of anomalies.

7 Conclusion

Our study focuses on Deep Feature Reconstruction (DFR), a memory- and compute-efficient method for detecting structural anomalies. We propose ULSAD, a unified framework that extends DFR to detect both structural and logical anomalies using a dual-branch architecture. In particular, we enhance the local branch's training objective to account for differences in the magnitude and direction of patch features, thereby improving structural anomaly detection. Additionally, we introduce an attention-based loss in the global branch to capture logical anomalies effectively. Extensive experiments on five benchmark image anomaly detection datasets demonstrate that `ULSAD` achieves competitive performance in anomaly detection and localization compared to eight state-of-the-art methods. Notably, `ULSAD` also performs well against memory-intensive, retrieval-based methods like PatchCore (Roth et al., 2022). Finally, ablation studies highlight the impact of various components in `ULSAD` and the role of the pre-trained backbone on overall performance.

Acknowledgment

This work is supported by the FLARACC research project (Federated Learning and Augmented Reality for Advanced Control Centers), funded by the Wallonia region in Belgium

Reproducibility Statement

We provide extensive descriptions of implementation details (in Section 4.1), algorithm (in Algorithm 1) and code to help readers reproduce our results. Every measure is taken to ensure fairness in our comparisons by adopting the most commonly adopted evaluation settings in the anomaly detection literature. More specifically, we use the Anomalib library for our experiments, whenever applicable, for comparing their performance with `ULSAD`. For methods such as DFR (Yang et al., 2020), which is not implemented in Anomalib, we refer to the original codebase provided by the authors.

Ethics Statement

We have read the TMLR Ethics Guidelines (https://jmlr.org/tmlr/ethics.html) and ensured that this work adheres to it. All benchmark datasets and pre-trained model checkpoints are publicly available and not directly subject to ethical concerns.

References

Charu C Aggarwal, Alexander Hinneburg, and Daniel A Keim. On the surprising behavior of distance metrics in high dimensional space. In *Database Theory—ICDT 2001: 8th International Conference London, UK, January 4–6, 2001 Proceedings 8*, pp. 420–434. Springer, 2001.

Mohiuddin Ahmed, Abdun Naser Mahmood, and Md Rafiqul Islam. A survey of anomaly detection techniques in financial domain. *Future Generation Computer Systems*, 55:278–288, 2 2016. ISSN 0167-739X. doi: 10.1016/J.FUTURE.2015.01.001.

Samet Akcay, Dick Ameln, Ashwin Vaidya, Barath Lakshmanan, Nilesh Ahuja, and Utku Genc. Anomalib: A Deep Learning Library for Anomaly Detection. In *2022 IEEE International Conference on Image Processing (ICIP)*, pp. 1706–1710. IEEE, 10 2022. ISBN 978-1-6654-9620-9. doi: 10.1109/ICIP46576.2022.9897283. URL https://ieeexplore.ieee.org/document/9897283/.

Mahmoud Assran, Quentin Duval, Ishan Misra, Piotr Bojanowski, Pascal Vincent, Michael Rabbat, Yann LeCun, and Nicolas Ballas. Self-supervised learning from images with a joint-embedding predictive architecture. In *Proceedings of the IEEE/CVF Conference on Computer Vision and Pattern Recognition*, pp. 15619–15629, 2023.

Kilian Batzner, Lars Heckler, and Rebecca König. EfficientAD: Accurate Visual Anomaly Detection at Millisecond-Level Latencies. In *Proceedings of the IEEE/CVF Winter Conference on Applications of Computer Vision (WACV)*, pp. 128–138, 1 2024. URL https://arxiv.org/abs/2303.14535v2.

Paul Bergmann, Michael Fauser, David Sattlegger, and Carsten Steger. MVTEC ad-A comprehensive real-world dataset for unsupervised anomaly detection. *Proceedings of the IEEE Computer Society Conference on Computer Vision and Pattern Recognition*, pp. 9584–9592, 2019. ISSN 10636919. doi: 10.1109/CVPR.2019.00982.

Paul Bergmann, Michael Fauser, David Sattlegger, and Carsten Steger. Uninformed Students: Student-Teacher Anomaly Detection With Discriminative Latent Embeddings. In *Proceedings of the IEEE/CVF Conference on Computer Vision and Pattern Recognition (CVPR)*, pp. 4183–4192, 2020. URL www.mvtec.com.

Paul Bergmann, Kilian Batzner, Michael Fauser, David Sattlegger, and Carsten Steger. Beyond Dents and Scratches: Logical Constraints in Unsupervised Anomaly Detection and Localization. *International Journal of Computer Vision*, 130(4):947–969, 2022. ISSN 1573-1405. doi: 10.1007/s11263-022-01578-9. URL https://doi.org/10.1007/s11263-022-01578-9.

Varun Chandola, Arindam Banerjee, and Vipin Kumar. Anomaly detection. *ACM Computing Surveys*, 41(3): 1–58, 7 2009. ISSN 0360-0300. doi: 10.1145/1541880.1541882. URL https://dl.acm.org/doi/10.1145/1541880.1541882.

Heejeong Choi, Donghwa Kim, Jounghee Kim, Jina Kim, and Pilsung Kang. Explainable anomaly detection framework for predictive maintenance in manufacturing systems. *Applied Soft Computing*, 125:109147, 8 2022. ISSN 1568-4946. doi: 10.1016/J.ASOC.2022.109147.

Thomas Defard, Aleksandr Setkov, Angelique Loesch, and Romaric Audigier. PaDiM: a Patch Distribution Modeling Framework for Anomaly Detection and Localization. In *International Conference on Pattern Recognition*, volume 12664 LNCS, pp. 475–489. Springer Science and Business Media Deutschland GmbH, 11 2021. ISBN 9783030687984. doi: 10.48550/arxiv.2011.08785. URL https://arxiv.org/abs/2011.08785v1.

Hanqiu Deng and Xingyu Li. Anomaly Detection via Reverse Distillation From One-Class Embedding. In *Proceedings of the IEEE/CVF Conference on Computer Vision and Pattern Recognition (CVPR)*, pp. 9737–9746, 2022.

Alexey Dosovitskiy and Thomas Brox. Generating images with perceptual similarity metrics based on deep networks. *Advances in neural information processing systems*, 29, 2016.

Alexey Dosovitskiy, Lucas Beyer, Alexander Kolesnikov, Dirk Weissenborn, Xiaohua Zhai, Thomas Unterthiner, Mostafa Dehghani, Matthias Minderer, Georg Heigold, Sylvain Gelly, Jakob Uszkoreit, and Neil Houlsby. An image is worth 16x16 words: Transformers for image recognition at scale. In *International Conference on Learning Representations*, 2021. URL https://openreview.net/forum?id=YicbFdNTTy.

Tharindu Fernando, Harshala Gammulle, Simon Denman, Sridha Sridharan, and Clinton Fookes. Deep learning for medical anomaly detection – a survey. *ACM Comput. Surv.*, 54(7), jul 2021. ISSN 0360-0300. doi: 10.1145/3464423. URL https://doi.org/10.1145/3464423.

Han Gao, Huiyuan Luo, Fei Shen, and Zhengtao Zhang. Towards Total Online Unsupervised Anomaly Detection and Localization in Industrial Vision, 5 2023. URL https://arxiv.org/abs/2305.15652v1.

Dong Gong, Lingqiao Liu, Vuong Le, Budhaditya Saha, Moussa Reda Mansour, Svetha Venkatesh, and Anton Van Den Hengel. Memorizing Normality to Detect Anomaly: Memory-augmented Deep Autoencoder for Unsupervised Anomaly Detection. *Proceedings of the IEEE International Conference on Computer Vision*, 2019-October:1705–1714, 4 2019. ISSN 15505499. doi: 10.48550/arxiv.1904.02639. URL https://arxiv.org/abs/1904.02639v2.

Denis Gudovskiy, Shun Ishizaka, and Kazuki Kozuka. CFLOW-AD: Real-Time Unsupervised Anomaly Detection with Localization via Conditional Normalizing Flows. *Proceedings - 2022 IEEE/CVF Winter Conference on Applications of Computer Vision, WACV 2022*, pp. 1819–1828, 7 2021. doi: 10.1109/WACV51458.2022.00188. URL https://arxiv.org/abs/2107.12571v1.

Waleed Hilal, S. Andrew Gadsden, and John Yawney. Financial Fraud: A Review of Anomaly Detection Techniques and Recent Advances. *Expert Systems with Applications*, 193:116429, 5 2022. ISSN 0957-4174. doi: 10.1016/J.ESWA.2021.116429.

Stepan Jezek, Martin Jonak, Radim Burget, Pavel Dvorak, and Milos Skotak. Deep learning-based defect detection of metal parts: Evaluating current methods in complex conditions. *International Congress on Ultra Modern Telecommunications and Control Systems and Workshops*, 2021-October:66–71, 2021. ISSN 2157023X. doi: 10.1109/ICUMT54235.2021.9631567.

Xi Jiang, Jianlin Liu, Jinbao Wang, Qiang Nie, Kai WU, Yong Liu, Chengjie Wang, and Feng Zheng. SoftPatch: Unsupervised Anomaly Detection with Noisy Data. *Advances in Neural Information Processing Systems*, 35: 15433–15445, 2022. URL https://github.com/TencentYoutuResearch/AnomalyDetection-SoftPatch.

Chieh-Hsin Lai, Dongmian Zou, and Gilad Lerman. Robust Subspace Recovery Layer for Unsupervised Anomaly Detection. *arXiv preprint*, 3 2019. doi: 10.48550/arxiv.1904.00152. URL https://arxiv.org/abs/1904.00152v2.

Sungwook Lee, Seunghyun Lee, and Byung Cheol Song. CFA: Coupled-hypersphere-based Feature Adaptation for Target-Oriented Anomaly Localization. *IEEE Access*, 10:78446–78454, 6 2022. ISSN 21693536. doi: 10.1109/ACCESS.2022.3193699. URL https://arxiv.org/abs/2206.04325v1.

Jiaqi Liu, Guoyang Xie, Jinbao Wang, Shangnian Li, Chengjie Wang, Feng Zheng, and Yaochu Jin. Deep industrial image anomaly detection: A survey. *Machine Intelligence Research*, 21(1):104–135, 2024.

Pankaj Mishra, Riccardo Verk, Daniele Fornasier, Claudio Piciarelli, and Gian Luca Foresti. VT-ADL: A Vision Transformer Network for Image Anomaly Detection and Localization. *IEEE International Symposium on Industrial Electronics*, 2021-June, 4 2021. doi: 10.1109/ISIE45552.2021.9576231. URL http://arxiv.org/abs/2104.10036http://dx.doi.org/10.1109/ISIE45552.2021.9576231.

Duc Tam Nguyen, Zhongyu Lou, Michael Klar, and Thomas Brox. Anomaly Detection With Multiple-Hypotheses Predictions. In Kamalika Chaudhuri and Ruslan Salakhutdinov (eds.), *Proceedings of the 36th International Conference on Machine Learning*, volume 97 of *Proceedings of Machine Learning Research*, pp. 4800–4809. PMLR, 7 2019. URL https://proceedings.mlr.press/v97/nguyen19b.html.

Guansong Pang, Chunhua Shen, Longbing Cao, and Anton van den Hengel. Deep Learning for Anomaly Detection: A Review. *ACM Computing Surveys*, 54(2), 7 2020. doi: 10.1145/3439950. URL http://arxiv.org/abs/2007.02500http://dx.doi.org/10.1145/3439950.

Adam Paszke, Sam Gross, Francisco Massa, Adam Lerer, James Bradbury Google, Gregory Chanan, Trevor Killeen, Zeming Lin, Natalia Gimelshein, Luca Antiga, Alban Desmaison, Andreas Köpf Xamla, Edward Yang, Zach Devito, Martin Raison Nabla, Alykhan Tejani, Sasank Chilamkurthy, Qure Ai, Benoit Steiner, Lu Fang Facebook, Junjie Bai Facebook, and Soumith Chintala. PyTorch: An Imperative Style, High-Performance Deep Learning Library. *Advances in Neural Information Processing Systems*, 32, 2019.

Pramuditha Perera, Ramesh Nallapati, and Bing Xiang. OCGAN: One-class novelty detection using gans with constrained latent representations. *Proceedings of the IEEE Computer Society Conference on Computer Vision and Pattern Recognition*, 2019-June:2893–2901, 6 2019. ISSN 10636919. doi: 10.1109/CVPR.2019.00301.

Lorenzo Perini, Vincent Vercruyssen, and Jesse Davis. Transferring the Contamination Factor between Anomaly Detection Domains by Shape Similarity. *Proceedings of the AAAI Conference on Artificial Intelligence*, 36(4):4128–4136, 6 2022. ISSN 2374-3468. doi: 10.1609/AAAI.V36I4.20331. URL https://ojs.aaai.org/index.php/AAAI/article/view/20331.

Lorenzo Perini, Paul-Christian Bürkner, and Arto Klami. Estimating the Contamination Factor's Distribution in Unsupervised Anomaly Detection. In *Proceedings of the 40th International Conference on Machine Learning*, pp. 27668–27679. PMLR, 7 2023. URL https://proceedings.mlr.press/v202/perini23a.html.

Tal Reiss, Niv Cohen, Eliahu Horwitz, Ron Abutbul, and Yedid Hoshen. Anomaly Detection Requires Better Representations. In *European Conference on Computer Vision*, pp. 56–68, 10 2022. ISBN 9783031250682. doi: 10.1007/978-3-031-25069-9{_}4. URL https://arxiv.org/abs/2210.10773v1.

Karsten Roth, Latha Pemula, Joaquin Zepeda, Bernhard Schölkopf, Thomas Brox, and Peter Gehler. Towards Total Recall in Industrial Anomaly Detection. In *Proceedings of the IEEE/CVF Conference on Computer Vision and Pattern Recognition*, pp. 14318–14328, 2022. doi: 10.48550/arxiv.2106.08265. URL https://arxiv.org/abs/2106.08265v2.

Lukas Ruff, Robert Vandermeulen, Nico Goernitz, Lucas Deecke, Shoaib Ahmed Siddiqui, Alexander Binder, Emmanuel Müller, and Marius Kloft. Deep One-Class Classification. In *International Conference on Machine Learning*, pp. 4393–4402. PMLR, 2018. URL https://proceedings.mlr.press/v80/ruff18a.html.

Lukas Ruff, Jacob R. Kauffmann, Robert A. Vandermeulen, Gregoire Montavon, Wojciech Samek, Marius Kloft, Thomas G. Dietterich, and Klaus Robert Muller. A Unifying Review of Deep and Shallow Anomaly Detection. *Proceedings of the IEEE*, 109(5):756–795, 5 2021. ISSN 15582256. doi: 10.1109/JPROC.2021.3052449.

Olga Russakovsky, Jia Deng, Hao Su, Jonathan Krause, Sanjeev Satheesh, Sean Ma, Zhiheng Huang, Andrej Karpathy, Aditya Khosla, Michael Bernstein, Alexander C. Berg, and Li Fei-Fei. ImageNet Large Scale Visual Recognition Challenge. *International Journal of Computer Vision*, 115(3):211–252, 12 2015. ISSN 15731405. doi: 10.1007/S11263-015-0816-Y/FIGURES/16. URL https://link.springer.com/article/10.1007/s11263-015-0816-y.

Mohammad Sabokrou, Mohammad Khalooei, Mahmood Fathy, and Ehsan Adeli. Adversarially Learned One-Class Classifier for Novelty Detection. *Proceedings of the IEEE Computer Society Conference on Computer Vision and Pattern Recognition*, pp. 3379–3388, 12 2018. ISSN 10636919. doi: 10.1109/CVPR.2018.00356.

Mohammadreza Salehi, Niousha Sadjadi, Soroosh Baselizadeh, Mohammad H. Rohban, and Hamid R. Rabiee. Multiresolution knowledge distillation for anomaly detection. *Proceedings of the IEEE Computer Society Conference on Computer Vision and Pattern Recognition*, pp. 14897–14907, 11 2021. ISSN 10636919. doi: 10.1109/CVPR46437.2021.01466. URL https://arxiv.org/abs/2011.11108v1.

Mohammadreza Salehi, Hossein Mirzaei, Dan Hendrycks, Yixuan Li, Mohammad Hossein Rohban, and Mohammad Sabokrou. A unified survey on anomaly, novelty, open-set, and out of-distribution detection: Solutions and future challenges. *Transactions on Machine Learning Research*, 2022. ISSN 2835-8856. URL https://openreview.net/forum?id=aRtjVZvbpK.

Wuqin Tang, Qiang Yang, Kuixiang Xiong, and Wenjun Yan. Deep learning based automatic defect identification of photovoltaic module using electroluminescence images. *Solar Energy*, 201:453–460, 5 2020. ISSN 0038-092X. doi: 10.1016/J.SOLENER.2020.03.049.

Robert Tibshirani and Trevor Hastie. Outlier sums for differential gene expression analysis. *Biostatistics*, 8 (1):2–8, 1 2007. ISSN 1465-4644. doi: 10.1093/BIOSTATISTICS/KXL005. URL https://academic.oup.com/biostatistics/article/8/1/2/252461.

Frederick Tung and Greg Mori. Similarity-preserving knowledge distillation. In *Proceedings of the IEEE/CVF international conference on computer vision*, pp. 1365–1374, 2019.

Siqi Wang, Yijie Zeng, Xinwang Liu, En Zhu, Jianping Yin, Chuanfu Xu, and Marius Kloft. Effective End-to-end Unsupervised Outlier Detection via Inlier Priority of Discriminative Network. *Advances in Neural Information Processing Systems*, 32, 2019.

Xudong Yan, Huaidong Zhang, Xuemiao Xu, Xiaowei Hu, and Pheng-Ann Heng. Learning Semantic Context from Normal Samples for Unsupervised Anomaly Detection. *Proceedings of the AAAI Conference on Artificial Intelligence*, 35(4):3110–3118, 5 2021. URL https://ojs.aaai.org/index.php/AAAI/article/view/16420.

Jie Yang, Yong Shi, and Zhiquan Qi. DFR: Deep Feature Reconstruction for Unsupervised Anomaly Segmentation. *Neurocomputing*, 424:9–22, 12 2020. doi: 10.1016/j.neucom.2020.11.018. URL http://arxiv.org/abs/2012.07122http://dx.doi.org/10.1016/j.neucom.2020.11.018.

Jinsung Yoon, Kihyuk Sohn, Chun-Liang Li, Sercan O. Arik, Chen-Yu Lee, and Tomas Pfister. Self-supervise, Refine, Repeat: Improving Unsupervised Anomaly Detection. *Transactions on Machine Learning Research (TMLR)*, 2022. URL https://arxiv.org/abs/2106.06115v2.

Jinsung Yoon, Kihyuk Sohn, Chun-Liang Li, Sercan O. Arik, and Tomas Pfister. SPADE: Semi-supervised Anomaly Detection under Distribution Mismatch. *Transactions on Machine Learning Research*, 11 2023. URL http://arxiv.org/abs/2212.00173.

Jiawei Yu, Ye Zheng, Xiang Wang, Wei Li, Yushuang Wu, Rui Zhao, and Liwei Wu. FastFlow: Unsupervised Anomaly Detection and Localization via 2D Normalizing Flows. *arXiv preprint arXiv:2111.07677*, 11 2021. doi: 10.48550/arxiv.2111.07677. URL https://arxiv.org/abs/2111.07677v2.

Sergey Zagoruyko and Nikos Komodakis. Wide Residual Networks. *British Machine Vision Conference 2016, BMVC 2016*, 2016-September:1–87, 5 2016. doi: 10.5244/C.30.87. URL https://arxiv.org/abs/1605.07146v4.

Sergey Zagoruyko and Nikos Komodakis. Paying more attention to attention: Improving the performance of convolutional neural networks via attention transfer. In *International Conference on Learning Representations*, 2017. URL https://openreview.net/forum?id=Sks9_ajex.

Vitjan Zavrtanik, Matej Kristan, and Danijel Skočaj. DRÆM - A discriminatively trained reconstruction embedding for surface anomaly detection. *Proceedings of the IEEE International Conference on Computer Vision*, pp. 8310–8319, 8 2021. ISSN 15505499. doi: 10.1109/ICCV48922.2021.00822. URL https://arxiv.org/abs/2108.07610v2.

Houssam Zenati, Chuan Sheng Foo, Bruno Lecouat, Gaurav Manek, and Vijay Ramaseshan Chandrasekhar. Efficient GAN-Based Anomaly Detection. *arXiv preprint*, 2 2018. doi: 10.48550/arxiv.1802.06222. URL https://arxiv.org/abs/1802.06222v2.

Jie Zhang, Masanori Suganuma, and Takayuki Okatani. Contextual Affinity Distillation for Image Anomaly Detection. *arXiv preprint arXiv:2307.03101*, 7 2023. URL https://arxiv.org/abs/2307.03101v1.

Kang Zhou, Yuting Xiao, Jianlong Yang, Jun Cheng, Wen Liu, Weixin Luo, Zaiwang Gu, Jiang Liu, and Shenghua Gao. Encoding Structure-Texture Relation with P-Net for Anomaly Detection in Retinal Images. In *European conference on computer vision*, volume 12365 LNCS, pp. 360–377. Springer, 2020. doi: 10.1007/978-3-030-58565-5{_}22. URL https://link.springer.com/10.1007/978-3-030-58565-5_22.

Yang Zou, Jongheon Jeong, Latha Pemula, Dongqing Zhang, and Onkar Dabeer. Spot-the-difference self-supervised pre-training for anomaly detection and segmentation. In *European Conference on Computer Vision*, pp. 392–408. Springer, 2022.

A Implementation Details

ULSAD is implemented in PyTorch (Paszke et al., 2019). Specifically, we used the Anomalib (Akcay et al., 2022) library by incorporating our code within it. It helps us have a fair comparison as we use the implementations of baselines from Anomalib. Moreover, we used a single NVIDIA A4000 GPU for all the experiments unless mentioned otherwise. The architecture of FRN and global autoencoder-like model is provided in Table 5 and 6, respectively.

Table 5: Feature Reconstruction Network of ULSAD.

	Layer Name	Stride	Kernel Size	Number of Kernels	Padding	Activation
Encoder	Conv-1	2	3×3	768	1	ReLU
	BatchNorm-1	-	-	-	-	-
	Conv-2	2	3×3	1536	1	ReLU
	BatchNorm-2	-	-	-	-	-
	Conv-3	1	3×3	1536	1	ReLU
	BatchNorm-3	-	-	-	-	-
Decoder	ConvTranspose-1	2	4×4	768	1	ReLU
	BatchNorm-4	-	-	-	-	-
	ConvTranspose-2	2	4×4	384	1	ReLU
	BatchNorm-5	-	-	-	-	-
	ConvTranspose-3	1	5×5	384	1	ReLU
	BatchNorm-6	-	-	-	-	-

Table 6: Global Autoencoder of ULSAD.

	Layer Name	Stride	Kernel Size	Number of Kernels	Padding	Activation
Encoder	Conv-1	2	4×4	32	1	ReLU
	BatchNorm-1	-	-	-	-	-
	Conv-2	2	4×4	32	1	ReLU
	BatchNorm-2	-	-	-	-	-
	Conv-3	2	4×4	64	1	ReLU
	BatchNorm-3	-	-	-	-	-
	Conv-4	2	4×4	64	1	ReLU
	BatchNorm-4	-	-	-	-	-
	Conv-5	2	4×4	64	1	ReLU
	BatchNorm-5	-	-	-	-	-
	Conv-6	1	8×8	64	1	ReLU
	BatchNorm-6	-	-	-	-	-
Decoder	Interpolate-1 (31, mode= "bilinear")	-	-	-	-	-
	Conv-1	1	4×4	64	2	ReLU
	BatchNorm-1	-	-	-	-	-
	Interpolate-2 (8, mode= "bilinear")	-	-	-	-	-
	Conv-2	1	4×4	64	2	ReLU
	BatchNorm-2	-	-	-	-	-
	Interpolate-3 (16, mode= "bilinear")	-	-	-	-	-
	Conv-3	1	4×4	64	2	ReLU
	BatchNorm-3	-	-	-	-	-
	Interpolate-4 (32, mode= "bilinear")	-	-	-	-	-
	Conv-4	1	4×4	64	2	ReLU
	BatchNorm-4	-	-	-	-	-
	Interpolate-5 (64, mode= "bilinear")	-	-	-	-	-
	Conv-5	1	4×4	64	2	ReLU
	BatchNorm-5	-	-	-	-	-
	Interpolate-6 (32, mode= "bilinear")	-	-	-	-	-
	Conv-6	1	3×3	64	1	ReLU
	BatchNorm-6	-	-	-	-	-
	Conv-7	1	3×3	384	1	ReLU

B Extended Results

Extended versions of the Table 1 and 2 are provided in Tables 7-21. It shows the performance of `ULSAD` per category of the benchmark datasets for anomaly detection and localization. Additionally, we provide a visual comparison of the generated anomaly maps using the MVTecLOCO dataset in Figure 9.

Table 7: Anomaly detection based on Image AUROC on MVTec dataset.

Category	CFLOW (2021)	DRÆM (2021)	FastFlow (2021	PaDiM (2021)	PatchCore (2022)	RD (2022)	DFR (2020)	EffAD (2024)	`ULSAD` (Ours)
bottle	**100.0**	94.6	98.57	99.37	**100.0**	98.10	94.92	**100.0**	**100.0** ± 0.00
cable	93.46	74.29	89.30	86.94	**98.54**	95.41	79.54	94.61	97.92 ± 0.18
capsule	91.74	65.46	86.04	88.43	**97.93**	81.01	96.01	95.57	94.61 ± 0.28
carpet	93.26	57.70	98.76	97.31	97.91	57.95	97.59	**99.70**	98.50 ± 0.17
grid	93.57	76.02	99.08	84.04	97.24	93.07	94.57	**100.0**	92.67 ± 1.20
hazelnut	**100.0**	84.43	81.57	86.07	**100.0**	99.82	**100.0**	93.39	99.93 ± 0.05
leather	99.97	79.31	**100.0**	99.66	**100.0**	42.39	99.46	99.92	**100.0** ± 0.00
metal_nut	**99.76**	45.06	94.53	96.92	99.61	67.20	93.06	99.34	98.88 ± 0.07
pill	90.73	44.65	87.53	88.52	94.35	54.66	92.06	**99.08**	96.17 ± 0.39
screw	88.30	89.38	66.00	75.24	**98.26**	94.57	93.69	98.09	95.20 ± 0.15
tile	**100.0**	90.15	95.42	95.49	98.67	97.37	92.97	99.85	99.99 ± 0.02
toothbrush	83.33	80.28	79.44	93.61	**100.0**	84.72	**100.0**	**100.0**	**100.0** ± 0.00
transistor	91.50	88.37	94.42	92.29	**100.0**	83.29	80.54	96.57	97.65 ± 0.57
wood	98.33	90.96	97.54	98.33	**99.30**	53.16	98.77	98.13	98.81 ± 0.23
zipper	93.07	68.17	92.54	86.48	**99.47**	92.04	89.97	99.22	94.36 ± 0.13
Mean	94.47	75.26	90.72	91.25	**98.75**	79.65	93.54	98.23	97.65 ± 0.38

Table 8: Anomaly segmentation performance based on Pixel AUROC on MVTec dataset.

Category	CFLOW (2021)	DRÆM (2021)	FastFlow (2021	PaDiM (2021)	PatchCore (2022)	RD (2022)	DFR (2020)	EffAD (2024)	`ULSAD` (Ours)
bottle	**98.58**	76.53	97.8	98.3	97.98	98.31	90.83	98.31	96.21 ± 2.21
cable	96.1	66.59	95.71	96.81	98.03	96.37	91.37	**98.5**	97.71 ± 0.06
capsule	98.71	86.96	98.37	98.67	98.77	**98.96**	98.46	98.33	98.95 ± 0.03
carpet	98.57	71.95	98.27	98.68	98.67	99.05	98.46	94.83	**99.18** ± 0.06
grid	97.49	53.56	98.39	92.82	97.86	**99.01**	97.41	96.02	95.47 ± 1.09
hazelnut	98.64	84.66	94.79	97.85	98.43	**98.91**	98.53	96.15	98.81 ± 0.03
leather	99.42	63.32	**99.62**	99.30	98.87	99.17	99.33	97.5	98.68 ± 0.01
metal_nut	97.97	80.25	97.01	96.71	**98.51**	97.68	93.02	98.07	97.62 ± 0.03
pill	97.83	77.17	96.38	95.03	97.53	96.96	96.86	**98.63**	96.67 ± 0.09
screw	97.64	83.38	89.87	97.89	99.19	**99.43**	99.07	98.50	99.33 ± 0.01
tile	**96.68**	85.75	93.14	92.42	94.86	95.47	90.82	91.61	95.78 ± 0.05
toothbrush	98.16	90.70	97.50	98.83	98.67	**98.99**	98.49	96.0	98.42 ± 0.02
transistor	89.91	63.23	96.45	96.85	96.84	86.77	79.11	94.77	**98.89** ± 0.05
wood	94.70	71.73	**95.71**	93.83	93.31	95.06	95.36	90.85	95.20 ± 0.31
zipper	97.08	69.31	97.62	97.82	98.06	**98.54**	96.85	96.21	97.24 ± 0.07
Mean	97.17	75.01	96.44	96.79	**97.71**	97.25	94.93	96.29	97.61 ± 0.64

Table 9: Anomaly segmentation performance based on Pixel AUPRO on MVTec dataset.

Category	CFLOW (2021)	DRÆM (2021)	FastFlow (2021	PaDiM (2021)	PatchCore (2022)	RD (2022)	DFR (2020)	EffAD (2024)	ULSAD (Ours)
bottle	94.19	50.05	92.0	95.11	92.28	**95.12**	83.14	93.84	90.16 ± 3.24
cable	85.85	28.58	86.65	89.65	90.77	90.32	83.09	**92.53**	88.63 ± 0.48
capsule	90.47	81.11	90.15	92.62	92.4	93.93	**96.33**	91.09	93.77 ± 0.16
carpet	92.64	48.64	94.63	95.59	92.7	**96.41**	95.47	90.99	96.39 ± 0.24
grid	90.52	17.71	93.95	82.52	89.46	**96.39**	91.15	93.14	83.3 ± 3.96
hazelnut	96.12	76.19	93.92	92.95	94.44	96.92	**97.17**	83.25	94.87 ± 0.3
leather	98.39	52.1	**99.06**	97.91	96.33	97.97	98.34	97.32	97.44 ± 0.01
metal_nut	88.97	35.79	85.89	90.45	91.9	**94.4**	87.01	92.97	91.58 ± 0.19
pill	93.67	64.26	91.0	93.88	93.92	94.76	95.86	**95.93**	94.5 ± 0.08
screw	90.25	53.22	68.6	92.14	95.39	**97.05**	95.96	96.04	96.45 ± 0.1
tile	**91.49**	58.48	81.01	78.32	79.64	88.4	79.36	83.54	87.82 ± 0.15
toothbrush	81.05	54.02	80.62	**93.52**	86.48	92.23	92.93	88.61	86.28 ± 0.46
transistor	78.75	51.37	88.92	89.04	**94.06**	75.05	64.25	82.82	91.61 ± 0.68
wood	90.5	45.29	**93.26**	91.39	85.08	92.69	92.48	76.16	91.34 ± 0.29
zipper	89.3	28.98	92.12	92.48	92.43	**95.18**	88.74	93.48	90.89 ± 0.35
Mean	90.14	49.72	88.79	91.17	91.15	**93.12**	89.42	90.11	91.67 ± 1.36

Table 10: Anomaly detection performance based on Image AUROC on MVTecLOCO dataset.

Category	CFLOW (2021)	DRÆM (2021)	FastFlow (2021	PaDiM (2021)	PatchCore (2022)	RD (2022)	DFR (2020)	EffAD (2024)	ULSAD (Ours)
breakfast_box	71.86	70.26	74.04	63.66	**85.24**	52.69	65.46	74.80	83.54 ± 0.23
juice_bottle	81.70	62.55	78.03	88.42	92.51	76.28	86.81	98.89	**97.12** ± 0.10
pushpins	73.43	51.32	61.20	61.30	75.54	50.72	72.68	80.58	**86.85** ± 0.94
screw_bag	65.48	59.39	68.04	60.14	69.90	65.15	63.55	67.42	**70.71** ± 1.49
splicing_connectors	75.63	68.25	73.71	68.40	**84.24**	62.95	75.87	81.39	82.30 ± 0.72
Mean	73.62	62.35	71.00	68.38	81.49	61.56	72.87	80.62	**84.1** ± 0.86

Table 11: Anomaly segmentation performance based on Pixel AUROC on MVTecLOCO dataset.

Category	CFLOW (2021)	DRÆM (2021)	FastFlow (2021	PaDiM (2021)	PatchCore (2022)	RD (2022)	DFR (2020)	EffAD (2024)	ULSAD (Ours)
breakfast_box	**89.6**	63.61	82.73	87.35	88.53	85.78	76.25	80.76	89.14 ± 0.11
juice_bottle	91.37	80.71	86.33	**91.99**	90.54	90.41	87.06	88.40	89.07 ± 0.10
pushpins	70.66	54.74	**82.94**	40.72	67.67	41.42	29.42	59.96	75.64 ± 0.36
screw_bag	69.94	65.23	58.07	65.35	62.40	67.33	59.74	61.64	**71.35** ± 0.12
splicing_connectors	63.40	54.16	67.69	71.20	69.71	57.82	56.14	61.02	**75.10** ± 0.20
Mean	76.99	63.69	75.55	71.32	75.77	68.55	61.72	70.36	**80.06** ± 0.20

Table 12: Anomaly segmentation performance based on Pixel AUPRO on MVTecLOCO dataset.

Category	CFLOW (2021)	DRÆM (2021)	FastFlow (2021	PaDiM (2021)	PatchCore (2022)	RD (2022)	DFR (2020)	EffAD (2024)	ULSAD (Ours)
breakfast_box	67.27	36.11	63.8	**74.28**	<u>73.08</u>	69.67	63.56	58.44	71.36 ± 0.38
juice_bottle	80.75	51.51	77.90	**88.78**	85.42	84.95	82.88	86.51	<u>87.72</u> ± 0.09
pushpins	61.09	24.68	50.62	52.71	<u>63.52</u>	53.52	59.12	59.25	**68.34** ± 0.55
screw_bag	54.39	31.27	38.1	61.42	56.12	59.66	**71.66**	62.45	<u>66.52</u> ± 0.33
splicing_connectors	71.15	56.72	34.77	62.64	67.29	63.62	<u>71.67</u>	68.14	**74.70** ± 0.25
Mean	66.93	40.06	53.04	67.97	69.09	66.28	<u>69.78</u>	66.96	**73.73** ± 0.35

Table 13: Anomaly detection performance based on Image AUROC on MPDD dataset.

Category	CFLOW (2021)	DRÆM (2021)	FastFlow (2021	PaDiM (2021)	PatchCore (2022)	RD (2022)	DFR (2020)	EffAD (2024)	ULSAD (Ours)
tubes	**99.64**	61.28	89.36	56.48	87.50	89.67	94.47	<u>95.28</u>	93.39 ± 0.57
metal_plate	97.42	80.05	86.92	42.69	<u>99.72</u>	91.87	68.31	**100.0**	93.81 ± 0.28
connector	<u>99.52</u>	83.33	52.38	86.07	**100.0**	93.10	**100.0**	50.00	96.00 ± 0.82
bracket_white	79.89	84.00	50.78	80.33	89.67	83.67	54.55	<u>96.48</u>	**100.0** ± 0.00
bracket_black	**96.48**	65.36	62.83	66.69	86.97	50.73	72.63	85.45	<u>93.09</u> ± 0.32
bracket_brown	49.70	70.81	47.89	78.66	<u>95.78</u>	68.70	88.54	85.32	**98.08** ± 0.14
Mean	87.11	74.14	65.03	68.48	<u>93.27</u>	79.62	79.75	85.42	**95.73** ± 0.45

Table 14: Anomaly segmentation performance based on Pixel AUROC on MPDD dataset.

Category	CFLOW (2021)	DRÆM (2021)	FastFlow (2021	PaDiM (2021)	PatchCore (2022)	RD (2022)	DFR (2020)	EffAD (2024)	ULSAD (Ours)
tubes	**99.15**	76.87	98.44	91.35	98.45	<u>99.08</u>	98.62	98.98	98.55 ± 0.10
metal_plate	**98.56**	96.23	92.99	91.67	<u>98.30</u>	97.50	93.59	96.52	96.77 ± 0.09
connector	97.38	90.01	92.69	97.93	99.11	98.55	98.68	<u>99.32</u>	**99.40** ± 0.18
bracket_white	96.74	86.64	90.23	97.21	97.90	<u>98.13</u>	96.63	97.71	**98.73** ± 0.1
bracket_black	<u>97.68</u>	95.89	94.39	93.79	97.52	96.40	**98.42**	97.17	97.43 ± 0.21
bracket_brown	95.04	76.11	92.84	95.13	97.15	<u>97.34</u>	**98.06**	92.46	93.83 ± 2.41
Mean	97.42	86.96	93.60	94.51	**98.07**	<u>97.83</u>	97.33	97.03	97.45 ± 0.99

Table 15: Anomaly segmentation performance based on Pixel AUPRO on MPDD dataset.

Category	CFLOW (2021)	DRÆM (2021)	FastFlow (2021	PaDiM (2021)	PatchCore (2022)	RD (2022)	DFR (2020)	EffAD (2024)	ULSAD (Ours)
tubes	**96.76**	44.84	94.85	71.53	93.83	95.98	95.20	<u>96.27</u>	94.33 ± 0.33
metal_plate	91.53	82.83	74.62	75.47	**92.50**	<u>92.00</u>	83.99	83.59	90.07 ± 0.22
connector	91.32	72.06	76.98	92.74	96.89	95.29	95.60	<u>97.77</u>	**97.98** ± 0.60
bracket_white	78.66	69.13	49.65	81.16	83.13	84.71	77.02	<u>93.27</u>	**95.33** ± 0.37
bracket_black	89.48	93.12	79.65	83.51	<u>93.65</u>	89.14	**95.57**	89.98	90.17 ± 0.67
bracket_brown	83.62	58.29	85.62	82.69	85.07	<u>94.04</u>	**95.37**	81.77	84.24 ± 6.38
Mean	88.56	70.04	76.89	81.18	90.84	<u>91.86</u>	90.46	90.44	**92.02** ± 2.64

Table 16: Anomaly detection performance based on Image AUROC on BTAD dataset.

Category	CFLOW (2021)	DRÆM (2021)	FastFlow (2021	PaDiM (2021)	PatchCore (2022)	RD (2022)	DFR (2020)	EffAD (2024)	ULSAD (Ours)
01	98.64	80.17	94.46	<u>99.51</u>	98.09	92.23	<u>99.51</u>	94.15	**100.0** ± 0.00
02	82.12	65.23	84.27	82.17	81.73	61.73	<u>85.68</u>	75.42	**88.5** ± 0.78
03	<u>99.95</u>	74.87	96.3	97.92	**100.0**	97.65	98.62	95.22	**100.0** ± 0.00
Mean	93.57	73.42	91.68	93.20	93.27	83.87	<u>94.60</u>	88.26	**96.17** ± 0.45

Table 17: Anomaly segmentation performance based on Pixel AUROC on BTAD dataset.

Category	CFLOW (2021)	DRÆM (2021)	FastFlow (2021	PaDiM (2021)	PatchCore (2022)	RD (2022)	DFR (2020)	EffAD (2024)	ULSAD (Ours)
01	95.44	59.11	93.05	96.54	95.94	**96.98**	<u>96.93</u>	64.59	95.86 ± 0.03
02	94.81	69.29	96.16	95.11	95.18	**96.83**	<u>96.77</u>	85.67	94.76 ± 0.88
03	99.55	48.73	99.25	<u>99.56</u>	99.44	**99.74**	99.12	96.12	99.55 ± 0.02
Mean	96.60	59.04	96.15	97.07	96.85	**97.85**	<u>97.62</u>	82.13	96.73 ± 0.51

Table 18: Anomaly segmentation performance based on AUPRO on BTAD dataset.

Category	CFLOW (2021)	DRÆM (2021)	FastFlow (2021	PaDiM (2021)	PatchCore (2022)	RD (2022)	DFR (2020)	EffAD (2024)	ULSAD (Ours)
01	66.79	21.57	60.83	75.76	64.34	<u>79.45</u>	**83.77**	29.75	72.88 ± 0.12
02	54.32	27.64	**67.98**	59.19	52.36	<u>66.05</u>	65.58	44.37	55.16 ± 6.83
03	98.21	18.24	96.99	<u>98.45</u>	97.76	**98.92**	27.83	88.98	98.18 ± 0.08
Mean	73.11	22.48	75.27	<u>77.80</u>	71.48	**81.47**	59.06	54.37	75.41 ± 3.95

Table 19: Anomaly detection performance based on Image AUROC on VisA dataset.

Category	CFLOW (2021)	DRÆM (2021)	FastFlow (2021	PaDiM (2021)	PatchCore (2022)	RD (2022)	DFR (2020)	EffAD (2024)	ULSAD (Ours)
candle	<u>94.38</u>	79.43	93.18	86.19	**98.59**	85.54	89.65	80.52	87.11 ± 0.29
capsules	69.9	72.77	<u>81.05</u>	61.72	69.92	**87.37**	76.75	63.73	79.61 ± 0.72
cashew	94.7	95.5	87.78	90.94	**96.29**	85.38	93.80	<u>96.11</u>	94.72 ± 0.16
chewinggum	99.02	83.68	95.18	98.20	<u>99.29</u>	81.92	99.22	98.27	**99.49** ± 0.12
fryum	92.98	70.46	92.60	85.06	93.5	77.94	**96.58**	95.70	<u>95.86</u> ± 0.14
macaroni1	92.72	72.8	82.48	78.62	91.50	82.06	<u>95.14</u>	**95.23**	90.66 ± 0.76
macaroni2	63.44	47.85	69.75	70.05	71.36	81.75	**86.25**	<u>83.82</u>	82.84 ± 1.05
pcb1	91.06	72.27	88.07	87.59	<u>95.08</u>	92.60	**97.57**	93.78	92.92 ± 0.11
pcb2	79.95	91.17	86.47	83.20	92.46	87.57	91.55	**94.95**	<u>93.67</u> ± 0.18
pcb3	82.23	81.29	81.47	72.79	92.46	90.87	**97.27**	<u>95.92</u>	93.62 ± 0.16
pcb4	96.29	90.44	95.68	95.67	<u>99.20</u>	96.17	97.62	97.89	**99.43** ± 0.03
pipe_fryum	96.54	75.32	96.16	89.28	98.07	85.68	98.36	<u>98.59</u>	**99.61** ± 0.11
Mean	87.77	77.75	87.49	83.28	<u>91.48</u>	86.24	85.18	91.21	**92.46** ± 0.45

Table 20: Anomaly segmentation performance based on Pixel AUROC on VisA dataset.

Category	CFLOW (2021)	DRÆM (2021)	FastFlow (2021	PaDiM (2021)	PatchCore (2022)	RD (2022)	DFR (2020)	EffAD (2024)	ULSAD (Ours)
candle	98.75	83.1	97.24	97.68	98.92	**99.11**	98.41	89.93	97.77 ± 0.03
capsules	96.88	62.39	97.13	90.60	97.62	**99.56**	99.13	96.93	98.31 ± 0.31
cashew	99.25	74.17	98.57	97.45	98.88	97.23	95.63	98.85	**99.49** ± 0.02
chewinggum	99.02	84.11	98.83	98.82	98.72	**99.37**	99.16	98.69	98.10 ± 0.41
fryum	97.08	85.7	93.20	96.20	94.30	96.33	95.45	96.52	**97.38** ± 0.19
macaroni1	98.71	63.95	98.60	97.85	98.13	99.48	**99.73**	99.59	99.00 ± 0.13
macaroni2	97.35	79.02	94.65	95.40	96.79	99.33	**99.43**	98.84	98.20 ± 0.28
pcb1	99.05	27.98	99.29	98.67	99.47	**99.65**	99.30	98.98	99.61 ± 0.01
pcb2	96.40	59.49	97.12	98.12	97.72	98.28	96.13	**98.37**	98.03 ± 0.09
pcb3	97.23	76.43	97.04	98.06	98.13	**98.98**	97.99	98.91	98.45 ± 0.05
pcb4	97.97	83.42	97.51	97.00	97.83	**98.29**	96.58	95.49	95.22 ± 0.27
pipe_fryum	98.79	75.99	98.72	99.19	98.68	98.6	97.97	98.99	**99.29** ± 0.03
Mean	98.04	71.31	97.32	97.09	97.93	**98.68**	97.90	97.51	98.24 ± 0.20

Table 21: Anomaly segmentation performance based on AUPRO on VisA dataset.

Category	CFLOW (2021)	DRÆM (2021)	FastFlow (2021	PaDiM (2021)	PatchCore (2022)	RD (2022)	DFR (2020)	EffAD (2024)	ULSAD (Ours)
candle	92.7	80.29	91.65	92.77	94.08	95.30	**95.56**	77.31	92.49 ± 0.15
capsules	74.64	34.4	81.8	48.42	68.88	**92.20**	92.09	83.8	82.76 ± 1.18
cashew	**93.0**	48.33	85.54	82.36	88.01	91.81	90.51	91.57	91.85 ± 1.15
chewinggum	**89.58**	62.66	84.69	84.33	83.86	88.57	85.52	74.87	84.34 ± 1.0
fryum	85.62	71.94	72.39	75.54	78.25	84.8	**92.08**	82.93	85.47 ± 0.66
macaroni1	89.46	63.37	91.89	88.55	91.74	95.53	**97.59**	96.06	92.8 ± 0.74
macaroni2	78.74	56.69	71.94	75.76	87.49	94.01	**94.23**	89.74	88.29 ± 1.89
pcb1	87.24	27.43	85.89	86.39	89.07	**95.0**	93.55	90.53	90.22 ± 0.28
pcb2	77.83	33.99	77.99	83.68	83.00	89.17	87.26	**90.43**	84.53 ± 0.53
pcb3	75.03	71.9	71.33	81.37	79.69	90.89	**92.48**	92.08	85.86 ± 0.38
pcb4	86.53	73.26	83.41	82.47	84.91	**89.17**	84.38	75.25	73.37 ± 0.81
pipe_fryum	93.14	31.86	81.89	87.99	92.42	94.76	**95.46**	68.77	93.49 ± 0.08
Mean	85.29	54.68	81.70	80.80	85.12	**91.77**	91.72	84.45	87.12 ± 0.89

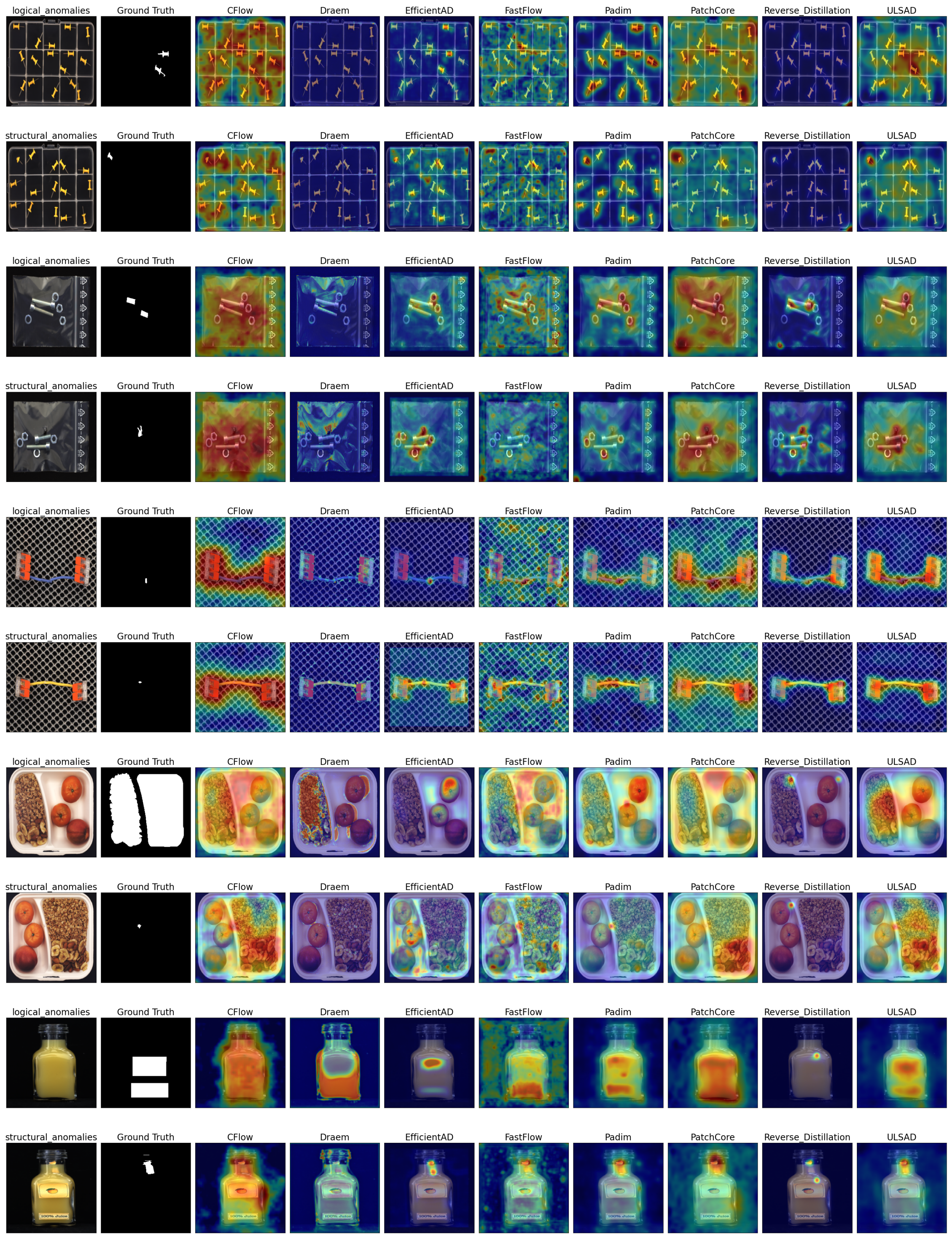

Figure 9: Visualization of anomaly maps on anomalous images from MVTecLOCO dataset.

B.1 Performance on MVTecLOCO: Logical and Structural AD

In Tables 22, 23, 24, 25, 26, and 27, we report the anomaly detection and localization results on MVTec LOCO separately for structural and logical anomalies. It can be observed that although PatchCore performs slightly better than `ULSAD` on structural anomalies, `ULSAD` delivers competitive results on logical anomalies. Moreover, as discussed previously in Section 5, the improvement in performance with PatchCore comes with three times the memory requirement. Therefore, we consider `ULSAD` to be an efficient and effective approach for the detection and localization of both logical and structural anomalies.

Table 22: Anomaly detection performance based on Image AUROC on **structural anomalies** of MVTecLOCO dataset.

Category	CFLOW (2021)	DRÆM (2021)	FastFlow (2021	PaDiM (2021)	PatchCore (2022)	RD (2022)	DFR (2020)	EffAD (2024)	`ULSAD` (Ours)
breakfast_box	62.3	75.37	71.67	64.17	**84.3**	48.74	58.67	69.04	81.94 ± 0.74
juice_bottle	73.45	52.18	76.52	86.17	96.47	78.29	62.75	**99.71**	95.53 ± 0.45
pushpins	71.03	66.51	60.17	72.4	77.42	50.17	40.06	**92.07**	85.17 ± 0.65
screw_bag	78.0	69.78	75.07	67.7	**86.79**	80.35	57.76	82.2	83.01 ± 1.56
splicing_connectors	74.35	80.33	70.31	66.85	88.67	63.04	55.84	**90.2**	80.59 ± 0.35
Mean	71.83	68.83	70.75	71.46	**86.73**	64.12	55.02	86.64	85.25 ± 0.86

Table 23: Anomaly segmentation performance based on Pixel AUROC on **structural anomalies** of MVTecLOCO dataset.

Category	CFLOW (2021)	DRÆM (2021)	FastFlow (2021	PaDiM (2021)	PatchCore (2022)	RD (2022)	DFR (2020)	EffAD (2024)	`ULSAD` (Ours)
breakfast_box	94.72	61.6	84.86	88.41	94.31	91.75	82.79	67.36	**95.35** ± 0.16
juice_bottle	88.81	83.75	85.67	90.73	95.98	89.57	80.74	**97.24**	89.67 ± 0.23
pushpins	91.4	46.14	85.54	90.82	**95.16**	87.83	48.52	89.48	88.38 ± 0.22
screw_bag	95.37	72.27	91.74	94.97	97.45	**97.78**	66.67	97.37	97.64 ± 0.24
splicing_connectors	98.3	93.03	95.79	96.25	**98.82**	97.25	91.82	98.55	98.3 ± 0.1
Mean	93.72	71.36	88.72	92.24	**96.34**	92.84	74.12	90.0	93.87 ± 0.2

Table 24: Anomaly segmentation performance based on Pixel AUPRO on **structural anomalies** of MVTecLOCO dataset.

Category	CFLOW (2021)	DRÆM (2021)	FastFlow (2021	PaDiM (2021)	PatchCore (2022)	RD (2022)	DFR (2020)	EffAD (2024)	`ULSAD` (Ours)
breakfast_box	70.0	41.92	71.29	**81.97**	78.71	76.67	26.67	65.87	75.43 ± 0.67
juice_bottle	80.56	50.44	87.61	92.64	**95.1**	90.81	61.67	92.08	90.1 ± 0.31
pushpins	68.34	20.04	61.72	70.01	75.88	62.63	45.30	**78.62**	68.34 ± 0.84
screw_bag	82.07	39.41	73.69	85.1	88.92	**93.77**	53.95	91.38	91.98 ± 0.73
splicing_connectors	87.75	68.61	67.8	82.35	91.69	83.57	63.44	**94.19**	90.84 ± 0.35
Mean	77.74	44.08	72.42	82.41	**86.06**	81.49	50.21	84.43	83.34 ± 0.62

Table 25: Anomaly detection performance based on Image AUROC on **logical anomalies** of MVTecLOCO dataset.

Category	CFLOW (2021)	DRÆM (2021)	FastFlow (2021	PaDiM (2021)	PatchCore (2022)	RD (2022)	DFR (2020)	EffAD (2024)	ULSAD (Ours)
breakfast_box	76.86	68.71	75.81	62.0	<u>83.43</u>	55.27	61.55	**83.54**	83.33 ± 1.63
juice_bottle	80.52	70.09	80.89	92.94	94.61	76.4	77.07	**99.12**	<u>98.82</u> ± 0.14
pushpins	71.15	37.9	58.81	50.72	<u>74.53</u>	52.98	60.27	72.0	**85.23** ± 0.72
screw_bag	60.72	52.34	<u>64.01</u>	55.29	59.36	55.09	63.64	58.8	**66.33** ± 0.9
splicing_connectors	67.5	56.15	74.54	69.43	<u>80.27</u>	61.74	53.10	75.64	**86.27** ± 1.33
Mean	71.35	57.04	70.81	66.08	<u>78.44</u>	60.3	63.13	77.82	**84.0** ± 1.07

Table 26: Anomaly segmentation performance based on Pixel AUROC on **logical anomalies** of MVTecLOCO dataset.

Category	CFLOW (2021)	DRÆM (2021)	FastFlow (2021	PaDiM (2021)	PatchCore (2022)	RD (2022)	DFR (2020)	EffAD (2024)	ULSAD (Ours)
breakfast_box	<u>90.43</u>	65.5	85.35	89.23	90.32	87.35	74.55	85.58	**91.41** ± 0.1
juice_bottle	92.56	80.49	90.23	**95.29**	<u>93.97</u>	92.97	86.95	91.98	93.74 ± 0.08
pushpins	70.38	56.06	**82.91**	41.95	69.39	41.86	67.93	61.12	<u>75.96</u> ± 1.11
screw_bag	67.75	65.43	58.93	66.02	63.81	68.4	**75.75**	61.85	<u>72.3</u> ± 0.41
splicing_connectors	60.8	52.1	66.82	<u>69.83</u>	68.06	55.5	57.67	59.01	**74.19** ± 0.19
Mean	76.38	63.92	76.85	72.46	<u>77.11</u>	69.22	72.57	71.91	**81.52** ± 0.54

Table 27: Anomaly segmentation performance based on Pixel AUPRO on **logical anomalies** of MVTecLOCO dataset.

Category	CFLOW (2021)	DRÆM (2021)	FastFlow (2021	PaDiM (2021)	PatchCore (2022)	RD (2022)	DFR (2020)	EffAD (2024)	ULSAD (Ours)
breakfast_box	68.79	32.23	64.39	69.74	<u>72.27</u>	68.77	43.60	52.19	**73.97** ± 0.8
juice_bottle	79.67	52.72	77.9	<u>91.69</u>	87.88	84.22	62.87	87.82	**91.36** ± 0.12
pushpins	59.07	26.21	47.71	51.93	<u>63.47</u>	53.84	41.80	58.36	**68.78** ± 0.98
screw_bag	50.7	26.98	25.58	<u>53.92</u>	46.8	48.72	54.59	52.8	**61.48** ± 0.45
splicing_connectors	<u>65.86</u>	53.71	26.66	57.66	62.21	58.85	34.72	62.7	**72.66** ± 0.27
Mean	64.82	38.37	48.45	64.99	<u>66.53</u>	62.88	47.52	62.77	**73.65** ± 0.61

C Extended Ablations

In this section, we provide additional ablations on the local branch in Table 28 and the total architecture in Table 29. Lastly, in Table 30 we provide the per-category results for the ablation on the pre-trained backbone which is summarized in Figure 7.

Table 28: Abalations for local branch. Style: I-AUROC | P-AUROC | P-AUPRO.

category	$\lambda_l = 0$	$\lambda_l = 0.01$	$\lambda_l = 0.5$	$\lambda_l = 0.9$	$\lambda_l = 1.0$
breakfast_box	78.64 | 88.28 | 74.22	79.2 | **88.51** | **74.35**	77.86 | 87.79 | 71.27	77.95 | 86.89 | 67.06	**79.44** | 86.96 | 65.36
juice_bottle	**97.82** | 92.14 | 89.24	97.76 | **92.23** | 89.38	97.56 | 88.78 | 88.16	97.36 | 84.39 | 84.63	97.08 | 83.61 | 83.47
pushpins	72.4 | 69.81 | 65.69	72.77 | 69.84 | 65.68	**79.92** | **74.49** | **69.03**	76.98 | 74.35 | 63.17	76.53 | 73.69 | 65.18
screw_bag	66.42 | 66.6 | 64.39	67.18 | 68.47 | 65.92	**68.06** | 69.13 | **66.22**	67.56 | **69.33** | 63.61	66.34 | 69.31 | 62.09
splicing_connectors	**73.05** | 59.04 | 73.3	72.84 | 59.15 | 73.29	72.29 | 62.66 | 72.39	72.79 | 64.33 | 70.74	72.36 | **64.5** | 70.57
Mean	77.67 | 75.17 | 73.37	77.95 | 75.64 | **73.72**	**79.14** | **76.57** | 73.41	78.53 | 75.86 | 69.84	78.35 | 75.61 | 69.33

Table 29: Abalations for total architecture. Style: I-AUROC | P-AUROC | P-AUPRO.

category	$\mathcal{L}_{pg}^{d}$	$\mathcal{L}_{pg}^{d}$; $\mathcal{L}_{lg}$	$\mathcal{L}_{pg}$	$\mathcal{L}_{pg}$; $\mathcal{L}_{lg}$
$\lambda_l = \lambda_g = 0.0$				
breakfast_box	77.29 | **90.41** | 77.16	82.82 | 89.85 | 76.92	66.01 | 87.36 | 67.5	**85.08** | 90.19 | 75.36
juice_bottle	96.48 | **92.01** | 88.82	**97.93** | 91.82 | **89.26**	91.2 | 91.98 | 85.38	97.29 | 92.0 | 89.18
pushpins	70.89 | 80.89 | 70.67	**78.66** | **88.09** | **79.11**	74.67 | 77.37 | 58.75	74.61 | 85.86 | 76.33
screw_bag	65.48 | 65.87 | 64.04	63.02 | 68.13 | **65.51**	61.14 | 59.51 | 57.75	**66.93** | **68.67** | 65.35
splicing_connectors	78.29 | 69.68 | 75.61	**84.55** | 72.71 | **76.54**	65.31 | 53.4 | 66.74	81.5 | **73.11** | 76.01
Mean	77.69 | 79.77 | 75.26	**81.4** | **82.12** | **77.47**	71.67 | 73.92 | 67.22	81.08 | 81.97 | 76.45
$\lambda_l = \lambda_g = 0.5$				
breakfast_box	79.22 | **90.87** | **78.32**	82.45 | 88.49 | 71.03	71.36 | 87.64 | 67.38	**83.36** | 89.34 | 72.36
juice_bottle	96.3 | 91.17 | **88.89**	**98.08** | 87.06 | 88.05	91.14 | **91.84** | 85.92	97.46 | 88.81 | 87.71
pushpins	79.86 | 84.89 | 77.97	82.46 | **87.62** | **80.49**	78.64 | 81.14 | 65.12	**88.07** | 74.22 | 66.45
screw_bag	66.58 | 68.83 | 66.11	65.11 | 70.04 | 62.81	62.09 | 67.32 | 62.92	**70.6** | **71.58** | **67.01**
splicing_connectors	80.53 | 73.47 | **75.44**	**82.85** | 73.03 | 75.13	69.33 | 55.02 | 63.69	81.27 | **74.94** | 74.89
Mean	80.5 | **81.85** | **77.35**	82.19 | 81.25 | 75.5	74.51 | 76.59 | 69.01	**84.15** | 79.78 | 73.68

Table 30: Abalations for backbone on MvTec-LOCO. Style: I-AUROC | P-AUROC | P-AUPRO.

Class	ResNet50	ResNet152	Wide-ResNet50-2	Wide-ResNet100-2
breakfast_box	82.41 | 89.74 | 73.09	**85.11** | **91.15** | 72.0	84.46 | 89.18 | 72.21	82.37 | 89.25 | **74.02**
juice_bottle	96.9 | 92.23 | 89.38	97.64 | 91.66 | 89.78	97.11 | 88.9 | 87.94	**98.74** | **92.87** | **91.07**
pushpins	81.79 | **79.49** | **75.15**	73.28 | 76.49 | 63.71	**85.48** | 75.46 | 67.82	82.48 | 76.55 | 70.67
screw_bag	66.46 | 69.14 | **67.01**	68.06 | 68.63 | 66.97	71.14 | **71.57** | 66.82	**73.1** | 68.99 | 66.88
splicing_connectors	80.88 | 72.76 | 74.39	83.53 | 76.31 | 77.24	82.59 | 75.21 | 75.05	**84.71** | **79.95** | **78.65**
Mean	81.79 | 79.49 | 75.15	81.52 | 80.85 | 73.94	84.16 | 80.06 | 73.97	**84.28** | **81.52** | **76.26**